



ČVUT

**ČESKÉ VYSOKÉ
UČENÍ TECHNICKÉ
V PRAZE**



**FAKULTA
JADERNÁ
A FYZIKÁLNĚ
INŽENÝRSKÁ
ČVUT V PRAZE**

ISBN 978-80-01-07382-7

Vážený a milý Čtenáři.

Do rukou se ti dostává sborník studentských příspěvků prezentovaných na třinácté Studentské vědecké konferenci (SVK) fyziky pevných látek, fotoniky a materiálů. Konference se konala ve dnech 3. – 6. září 2024 pod tradiční pořadatelskou záštitou Katedry inženýrství pevných látek (KIPL) a nově i Katedry laserové fyziky a fotoniky (KLFF) Fakulty jaderné a fyzikálně inženýrské Českého vysokého učení v Praze (FJFI ČVUT) a uzavřela třináct těchto studentských odborných setkání organizovaných počínaje rokem 2011 každoročně (s jedinou pauzou v roce 2019) s laskavou podporou SVK grantů v rámci Studentského grantového systému (SGS) ČVUT.

Třináctý ročník konference se konal jak už tradičně v ověřeném a příjemném prostředí penzionu Kamínek, který se nachází v lokalitě Byňov nedaleko od Novohradských hor. Na konferenci bylo prezentováno celkem 24 příspěvků, z toho 13 studentských a 17 lektorských přednesených zvanými hosty z Akademie věd a společností CAN Superconductors, s. r. o. a On Semiconductor, s. r. o., pracovníky KIPLu, KLFF a KSI FJFI ČVUT. Témata prezentovaných studentských příspěvků pokryla řadu oblastí současné materiálové vědy, fyziky pevných látek, aplikované optiky, plasmoniky, nanovědy, fyzikální elektroniky, fyziky biomakromolekul a kvantových technologií. Vybrané příspěvky, které byly autory v termínu podány tvoří obsah tohoto sborníku, jehož četbu Ti milý Čtenáři vřele doporučuji.

Jako každoročně končím úvodní slovo poděkováním. V prvé řadě děkuji svým kolegům z organizačního výboru, který pracoval ve složení: tajemnice Kateřina Aubrechtová a Monika Kučeráková, členové Martin Dráb, Jiří Čapek, Karel Trojan, Milan Burda, Pavel Kwiecien, za výbornou a efektivní spolupráci, jejímž výsledkem byl celkově hladký průběh konference. Přednášejícím lektorům velmi děkuji za velmi kvalitní a inspirující příspěvky. A na závěr, „at last but not least“, adresuji poděkování všem zúčastněným studentům za jejich zajímavé a pečlivě připravené příspěvky představující výsledky jejich samostatné tvůrčí vědecké práce.

Všem studentům a spolupracovníkům přeji hodně invence a mnoho badatelských úspěchů do dalších let, a naší SVK pak úspěšné vkročení do druhého tuctu! :)

Za kolektiv organizátorů

Ladislav Kalvoda, vedoucí KIPL FJFI ČVUT v Praze

Obsah

Advances in Signal Processing, Automation and Construction of the Transient Grating Spectroscopy (J. Kušnír)	6
Tailoring of UNCD films with incorporated SiV centres (T. Meřová)	11
Preparation of protein single crystals for electron diffraction (N.V. Samochvalova)	16
Preparation of High-temperature YBCO Superconductors Thin Films Using Ionized Jet Deposition (M. Jůza)	22
Preparation and analysis of plasmonic Ag thin films deposited by Ionized Jet Deposition method and Magnetron Sputtering method (J. Lis)	28
MOVPE grown AlGaIn layers on sapphire substrates for UV applications (J. Batysta)	33
Optimisation of deposition parameters of Ionised Jet Deposition (IJD) created Titanium nitride thin films (M. Kolář)	39
AA bilayer coupler (P. Červenka)	47
The real structure of γ -Fe phase of rolled 1.4470 duplex steel after shot peening (M. Rušin)	54
Automated Image Analysis of exfoliated van der Waals material (J. Zelenka)	59

Advances in Signal Processing, Automation and Construction of the Transient Grating Spectroscopy

Jakub Kušnír¹

¹Department of Solid State Engineering, Faculty of Nuclear Sciences and Physical Engineering, Czech Technical University in Prague, Prague, Czech Republic
jakub.kusnir@cvut.cz

Abstract

Transient grating spectroscopy (TGS) is a non-destructive and non-contact optoacoustic method used to measure the elastic and thermal properties of solid materials. TGS can be used to measure samples over a wide range of temperatures. However, our TGS in its current design is not optimal for high and low-temperature measurements with sample rotation. The new TGS design, measurement automation and signal pre- and post-processing will be presented.

Keywords: Instruments, Transient Grating Spectroscopy, Elasticity, Thermal Diffusivity, Signal Processing

Introduction

Transient Grating Spectroscopy (TGS) [1-4] formerly known as Impulsive Stimulated Thermal Scattering (ISTS) [5-7] or also called Transient Thermal Grating (TTG) [8,9]. These methods were developed for non-destructive and contactless measurement of elastic and thermal properties of a broad range of solid materials. Choudhry *et al.* [9] discuss setup details and applications.

TGS is an optoacoustic method based on spatially periodic excitation and detection created as an interference pattern from two interfering detection or excitation beams on the sample surface. The interference creates many periodic line-like thermoelastic sources, leading to a strong constraint on spatial characteristics of the surface elastic and thermal response to a sudden excitation.

Heterodyne optical detection is used to increase the signal-to-noise ratio. Heterodyne detection is the combined diffraction of the detection beams on a transient grating formed on the sample surface after excitation with a reflection of detection beams from the surface, which is used as a reference for heterodyning. This leads to highly sensitive measurements of thermorefectance and surface-displacement dynamics [2,10].

This work is focused on possible improvements to the experimental setup of the TGS method to enable high-precision, low-noise, user-friendly and faster measurement of the samples over a wide temperature range.

Transient Grating Spectroscopy

Our TGS currently used for measurement is shown in (Figure 1) where all important components of the TGS experiment are present. A pulsed infrared laser is used for excitation and a green continuous laser for detection. Both laser beams travel through the same optical components.

First, the profile of both beams is deformed into ellipses by a cylindrical lens and then they are diffracted on transmission phase grating. From all the created diffraction beams, we use only +1 and -1 diffraction. These diffracted beams are projected by using a 4F imaging system onto the sample surface where they interfere. Heterodyned detection beams that are created and propagated from the sample surface are then separated by a polarizing cube and detected by a detector.

The main advantage of this TGS experiment is the possibility of sample rotation on the rotational stage. This allows us to measure the angular dispersion of acoustic waves on the sample surface. The velocity of these waves and their angular dispersion are then used in the inverse procedure described in [11-13] to determine elastic tensor. In addition, the time-domain signal can be used to determine thermal diffusivity as described in [14,15] and we observed apparent anisotropy of thermal diffusivity in cubic single crystals [16]. With a sample rotation, TGS can be used to determine the true anisotropy of thermal diffusivity for hexagonal or lower symmetries if good surface orientation is measured [14].

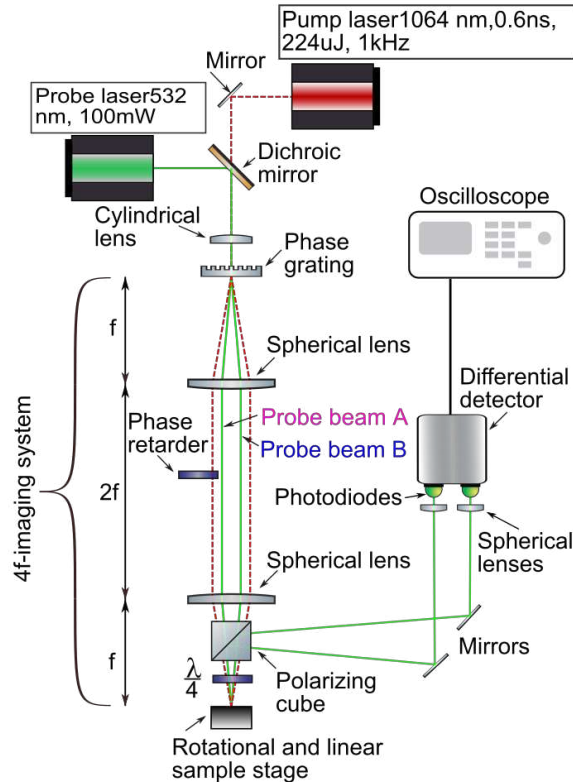


Figure 1: Top-view schematic of the TGS experiment.

The rotation of the sample is critical for the accurate determination of the elastic and thermal properties. This can easily be done in a room-temperature environment. However, for high or low temperatures when the sample is inside the temperature chamber, it is impractical or very hard to perfectly align the sample so that it is perpendicular to the optical axis during rotation with a heavy temperature chamber. Another problem is that there are no rotational stages small enough to be fitted inside the temperature chambers we own, do not have precise rotation or do not work in the temperature range we need.

Alternatively, we can try to rotate the whole TGS assembly, but this creates a similar problem with alignment and rotation as with the temperature chamber.

Our theoretical designs of the future TGS assembly led us to discover two possible and easy-to-implement methods for rotating the measurement direction using only the rotation of optical elements inside the TGS assembly. One setup was constructed and thoroughly tested.

Results

The first construction theoretically tested, was TGS with rotation of the transmission phase grating. If we rotate the phase grating by an angle θ from a horizontal position as illustrated in (Figure 1) will result in a rotation of measurement direction by an angle θ . Precise rotation of phase grating can be easily performed, and the sample needs to be only perpendicular to an optical axis.

However, heterodyne beams outgoing from the sample will rotate and de-rotation after the polarization cube will be required. If heterodyne beams are not de-rotated, we can measure both beams on one diode using a spherical lens or use a rotating detector or rotating beam blocker for one beam. De-rotation can be done with an optical component called a dove prism.

Dove prism is an optical component that rotates an image by 180° if the light is propagating along the longitudinal axis. Rotating the dove prism around the longitudinal axis by an angle θ creates $2*\theta$ image rotation. Another advantage is that if you send the rotated image back into the dove prism it de-rotates itself back to the original image. From this, we created a new theoretical TGS design illustrated in (Figure 2) that was built and tested.

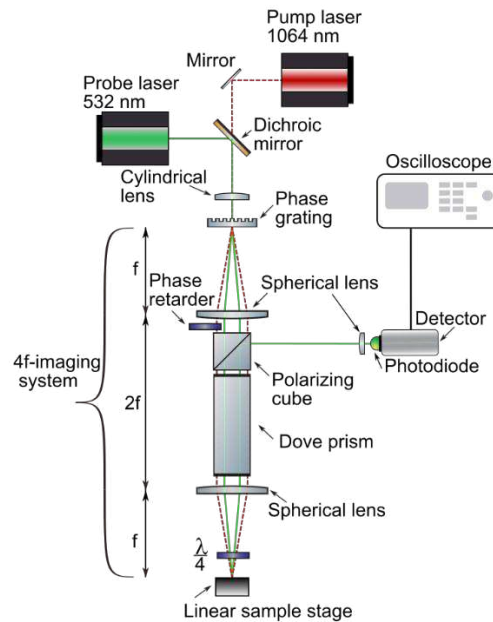


Figure 2: Top-view schematic of TGS experiment with a dove prism.

TGS with the dove prism was tested by measuring a single crystal of Ni with surface orientation (110). The results are shown in (Figure 3).

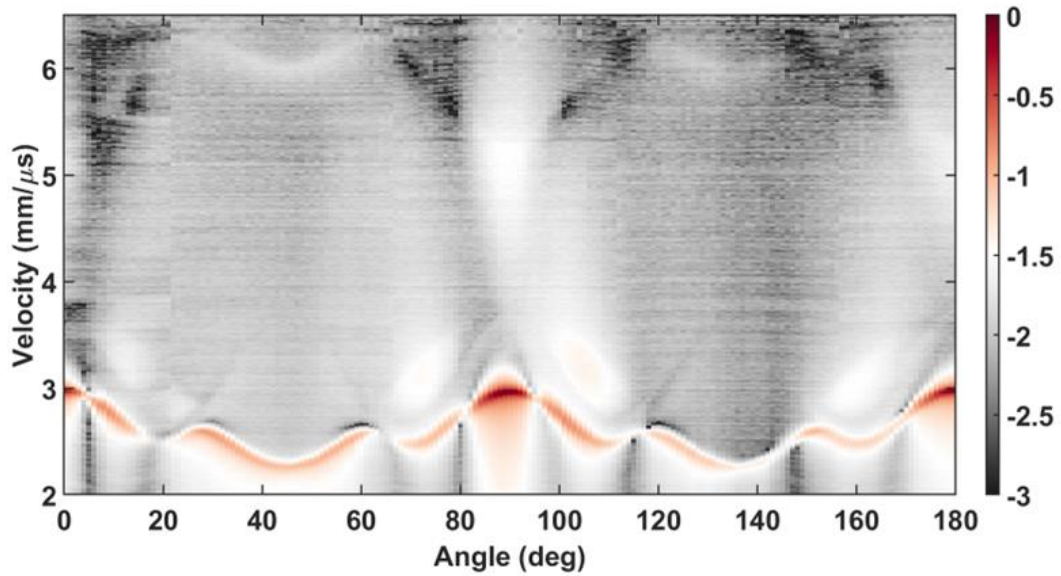


Figure 3: Velocity map of Ni (110) dependent on the dove prism angle of rotation.

Conclusion

We successfully created two new theoretical TGS assemblies with rotation of the measurement without sample rotation. TGS with the dove prism was found to be better and was constructed as illustrated in (Figure 2). The sample of single crystal Ni (110) was successfully measured.

The velocity map of the measured Ni (110) sample shown in (Figure 3) is good enough for the determination of elastic properties. All surface and limiting bulk waves are detected. However, measurement is not good for determination of the thermal diffusivity. We can observe some drops in velocity intensity. These drops in intensity result from the phase difference between beams propagating inside the dove prism. The phase difference is with high probability created because of the miss-alignment of the dove prism in a TGS assembly. For good measurement of the anisotropy of thermal diffusivity, we need stable and same phase difference for all measurement angles. We think this can be resolved by more testing and measuring by the new TGS with the dove prism.

References

- [1] J. A. Rogers, M. Fuchs, M. J. Banet, J. B. Hanselman, R. Logan, and K. A. Nelson, "Optical system for rapid materials characterization with the transient grating technique: Application to nondestructive evaluation of thin films used in microelectronics," *Appl. Phys. Lett.* 71, 225–227 (1997).
- [2] A. A. Maznev, K. A. Nelson, and J. A. Rogers, "Optical heterodyne detection of laser-induced gratings," *Opt. Lett.* 23, 1319–1321 (1998).
- [3] C. A. Dennett and M. P. Short, "Time-resolved, dual heterodyne phase collection transient grating spectroscopy," *Appl. Phys. Lett.* 110, 211106 (2017).
- [4] F. Hofmann, M. P. Short, and C. A. Dennett, "Transient grating spectroscopy: An ultrarapid, nondestructive materials evaluation technique," *MRS Bull.* 44, 392–402 (2019).

- [5] J. Sermeus, R. Sinha, K. Vanstreels, P. M. Vereecken, and C. Glorieux, “Determination of elastic properties of a MnO₂ coating by surface acoustic wave velocity dispersion analysis,” *J. Appl. Phys.* 116, 023503 (2014).
- [6] B. Verstraeten, J. Sermeus, R. Salenbien, J. Fizez, G. Shkerdin, and C. Glorieux, “Determination of thermoelastic material properties by differential heterodyne detection of impulsive stimulated thermal scattering,” *Photoacoustics* 3, 64–77 (2015).
- [7] T. Grabec, P. Sedlák, P. Stoklasová, M. Thomasová, D. Shilo, M. Kabla, H. Seiner, and M. Landa, “In-situ characterization of local elastic properties of thin shape memory films by surface acoustic waves,” *Smart Mater. Struct.* 25, 127002 (2016).
- [8] J. A. Johnson, J. K. Eliason, A. A. Maznev, T. Luo, and K. A. Nelson, “Non-diffusive thermal transport in GaAs at micron length scales,” *J. Appl. Phys.* 118, 155104 (2015).
- [9] U. Choudhry, T. Kim, M. Adams, J. Ranasinghe, R. Yang, and B. Liao, “Characterizing microscale energy transport in materials with transient grating spectroscopy,” *J. Appl. Phys.* 130, 231101 (2021).
- [10] J. A. Johnson, A. A. Maznev, M. T. Bulsara, E. A. Fitzgerald, T. C. Harman, S. Calawa, C. J. Vinels, G. Turner, and K. A. Nelson, “Phase-controlled, heterodyne laser-induced transient grating measurements of thermal transport properties in opaque material,” *J. Appl. Phys.* 111, 023503 (2012).
- [11] P. Stoklasová, P. Sedlák, H. Seiner, and M. Landa, “Forward and inverse problems for surface acoustic waves in anisotropic media: A Ritz–Rayleigh method based approach,” *Ultrasonics* 56, 381–389 (2015).
- [12] P. Stoklasová, T. Grabec, K. Zoubková, P. Sedlák, S. Krátký, and H. Seiner, “Laser-ultrasonic characterization of strongly anisotropic materials by transient grating spectroscopy,” *Exp. Mech.* 61, 663–676 (2021).
- [13] K. Zoubková, P. Stoklasová, T. Grabec, P. Sedlák, and H. Seiner, “Transient grating spectroscopy for complete elastic anisotropy: Beyond the measurement of surface acoustic waves,” in *2021 IEEE International Ultrasonics Symposium (IEEE, 2021)*.
- [14] O. W. Käding, H. Skurk, A. A. Maznev, and E. Matthias, “Transient thermal gratings at surfaces for thermal characterization of bulk materials and thin films,” *Appl. Phys. A Mater. Sci. Process.* 61, 253–261 (1995).
- [15] C. A. Dennett and M. P. Short, “Thermal diffusivity determination using heterodyne phase insensitive transient grating spectroscopy,” *J. Appl. Phys.* 123, 215109 (2018).
- [16] J. Kušnir, T. Grabec, K. Zoubková, P. Stoklasová, P. Sedlák, H. Seiner “Apparent anisotropic thermal diffusivity measured in cubic single crystals by transient grating spectroscopy,” *J. Appl. Phys.* 133 (12): 125108. (2023)

Acknowledgement

This work was supported by the Grant Agency of the Czech Technical University in Prague, grant No. SGS22/183/OHK4/3T/14.

Tailoring of UNCD films with incorporated SiV centres

Tímea Meřová¹, Kateřina Aubrechtová Dragounová¹, Alexander Kromka², Štěpán Potocký²

¹Department of Solid State Engineering, Faculty of Nuclear Sciences and Physical Engineering, Czech Technical University in Prague

²Department of Semiconductors, Institute of Physics of the Czech Academy of Sciences
melovtim@fjfi.cvut.cz

Abstract

Ultrananocrystalline diamond (UNCD) films incorporating photoluminescent color centres have emerged as promising materials for quantum sensing applications due to their unique optical properties. This study investigates the synthesis, characterization, and enhancement of silicon-vacancy (SiV) centres in UNCD films. We successfully fabricated variously Si-doped diamond films using microwave plasma chemical vapour deposition (MWPECVD). To enhance the photoluminescence (PL) of SiV centres, we employed oxidation treatment, which resulted in increased PL intensity compared to as-grown samples. Additionally, we utilized molten salt thermal etching (MSTE) to create nanoparticles from UNCD film, resulting in selective etching of the graphite phase while preserving nanocrystalline diamond particles with SiV PL. Surface characterization of the as-grown samples using contact angle measurements with deionized water droplets confirmed their hydrophobic nature. Our findings demonstrate a multi-faceted approach to UNCD growth and modification, offering controllable porous character and SiV center concentrations, and pave the way for advanced quantum sensing applications.

Keywords: Si-V centres; Photoluminescence; CVD; UNCD.

Introduction

Diamond's exceptional properties have positioned it as a frontrunner in advanced optical applications, particularly in the burgeoning field of diamond photonics. The discovery of optically active defects, such as silicon-vacancy (SiV) centres, has opened new avenues in quantum information processing, optical sensing, and biological marking.

This research delves into the preparation and characterization of diamond nano-porous structures, with a focus on ultra-nanocrystalline diamond (UNCD) films containing SiV centres. These films, featuring diamond crystals smaller than 10 nm, offer unique advantages for nanoscale optical devices due to their low surface roughness, minimal photobleaching, and short decay times. Using microwave plasma enhanced chemical vapor deposition (MWPECVD), we synthesized Si-doped UNCD films with incorporated SiV centres. Our study employed advanced optical measurement techniques to investigate the early growth stages of these films and evaluate the impact of various growth conditions and post-deposition treatments on their structure and optical properties.

The research aims to enhance the creation and optimization of active SiV centres in nanostructured diamond films, while developing nanoporous diamond films through innovative methods such as air annealing and molten salt thermal etching (MSTE). The latter approach holds promise for generating highly porous structures that can be easily disintegrated into individual diamond nanoparticles.

By combining synthesis, characterization, and optimization techniques, this work contributes to the advancement of diamond-based quantum technologies and bio-imaging applications.

Experiment

Silicon-doped UNCD films were grown on polished silicon substrates. The substrates were cleaned and treated with ultradispersed detonation diamond powder before growth. The diamond films were grown using MWPECVD in a hydrogen-rich plasma from CH₄, with the addition of N₂ and SiH₄. Methane serves as the carbon source, while nitrogen promotes UNCD film growth. Silane controls the incorporation of Si atoms into the UNCD films. UNCD films grown without silane can also reveal SiV centers due to etching of silicon substrates and reactor parts by reactive species, mainly atomic hydrogen.

Deposition conditions included a total gas pressure of 90 mbar, total gas flow of 300 sccm, microwave power of 4 kW, substrate temperature of 800°C, and deposition time of 8 hours. The gas mixture consisted of H₂/CH₄/N₂/SiH₄, with 3% methane and 1.5% nitrogen. SiH₄ flow was varied to achieve different SiV concentrations.

To create nanoporous structures, a MSTE process was implemented using lithium nitrate (LiNO₃). This process selectively etches defective areas on the diamond. MSTE conditions included 50 mg of LiNO₃ per sample, annealed at 450°C for 30 minutes. Post-treatment cleaning involved ultrasonic agitation in hydrochloric acid solution followed by rinsing with deionized water.

Results and discussion

SEM analysis revealed distinct morphological changes in UNCD films with varying Si/C ratios and after MSTE treatment. Fig. 1 shows a cross-section of undoped and 500 ppm doped samples and revealed a slight decrease in film thickness with SiH₄ addition, suggesting changes in plasma chemistry. Fig. 2 shows a slight shift to "needle-like" diamond grains post-MSTE for undoped sample and Si-doped samples exhibited a cauliflower-like surface morphology, which remained unchanged after MSTE. MSTE treatment increased film porosity due to selective etching of sp²-bonded carbon atoms, resulting in a visible change from greyish to dark black, indicating enhanced light absorption [1].

These observations highlight the significant impact of Si doping and MSTE treatment on UNCD film morphology, porosity, and growth characteristics.

Raman spectra of UNCD films with varying Si/C ratios were analyzed to confirm sample homogeneity and characterize their structure. The spectra in Fig. 3 revealed several key features typical of UNCD films for a doped sample. A diamond peak at approximately 1332 cm⁻¹ indicated the presence of sp³-bonded carbon, while a D-band at around 1340 cm⁻¹ represented the disordered graphitic phase. Two additional peaks at about 1150 cm⁻¹ and 1460 cm⁻¹ were attributed to trans-polyacetylene chains at grain boundaries, confirming the presence of nanometer-sized crystalline grains. The G-band, observed at approximately 1585 cm⁻¹, suggested the existence of sp²-bonded carbon structures [2]. These features collectively demonstrated the coexistence of sp³ and sp² carbon phases in the UNCD films. Notably, the consistency of spectra across different positions on the samples confirmed their morphological and chemical homogeneity [3].

These observations highlight the significant impact of Si doping and MSTE treatment on UNCD film morphology, porosity, and growth characteristics. Raman spectra of UNCD films with varying Si/C ratios were analyzed to confirm sample homogeneity and characterize their structure. The spectra in Fig. 3 revealed several key features typical of UNCD films for a doped sample. A diamond peak at approximately 1332 cm⁻¹ indicated the presence of sp³-bonded carbon, while a

D-band at around 1340 cm^{-1} represented the disordered graphitic phase. Two additional peaks at about 1150 cm^{-1} and 1460 cm^{-1} were attributed to trans-polyacetylene chains at grain boundaries, confirming the presence of nanometer-sized crystalline grains. The G-band, observed at approximately 1585 cm^{-1} , suggested the existence of sp^2 -bonded carbon structures [2]. These features collectively demonstrated the coexistence of sp^3 and sp^2 carbon phases in the UNCD films. Notably, the consistency of spectra across different positions on the samples confirmed their morphological and chemical homogeneity [3].

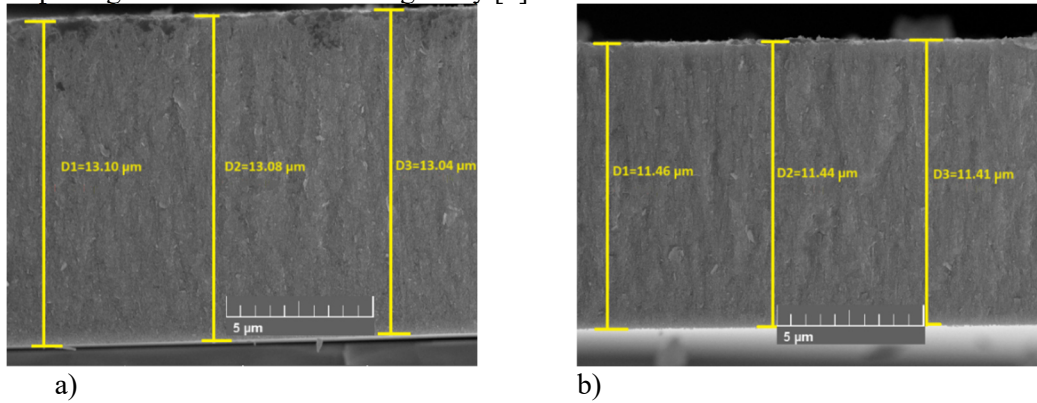


Fig. 1 SEM images of cross-sections for UNCD films deposited at a) 0 ppm, b) 500 ppm

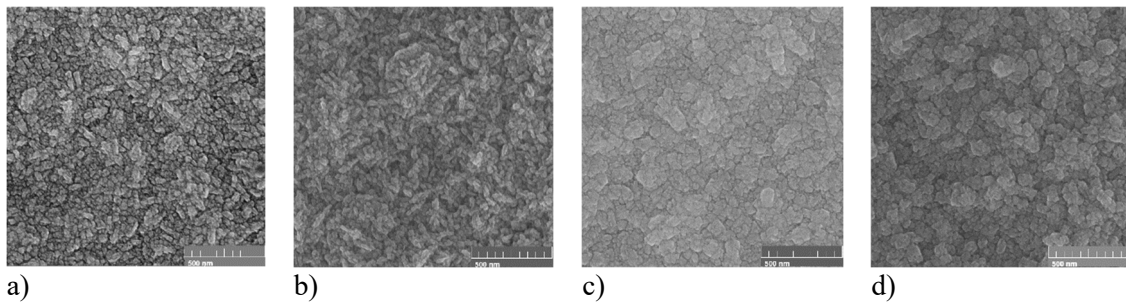


Fig. 2 SEM images of surfaces of samples with 0 ppm and 500 ppm Si/C concentrations (a), (c) as-grown (b), (d) after MSTE process with 10 mg of LiNO_3 , the scale bar 500 nm.

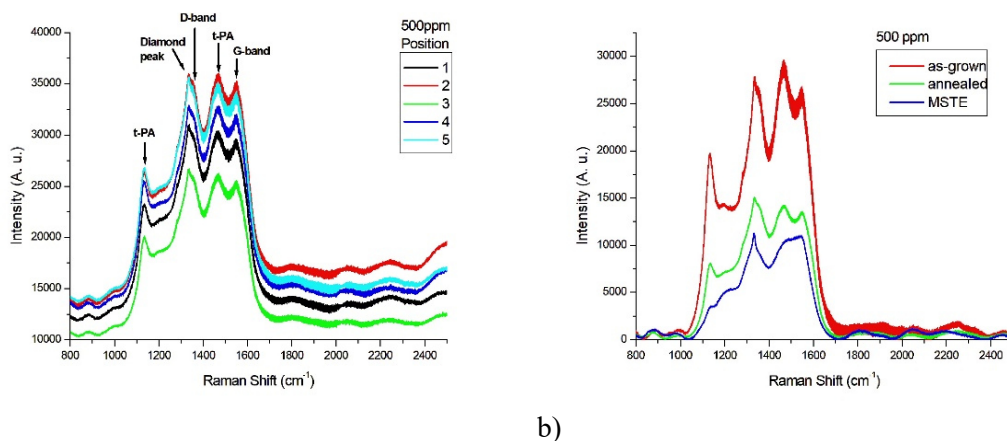


Fig. 3 Raman spectra of UNCD film doped with 500 ppm Si/C concentration a) collected from 5 different positions, b) for as-grown, annealed and MSTE samples

PL measurements of Si-doped UNCD films revealed a characteristic peak at approximately 738 nm, corresponding to the zero phonon line (ZPL) of SiV centers [4]. This confirmed the successful incorporation of silicon-based color centers during the CVD growth process. Two additional peaks at 602.69 nm and 629 nm were observed, though their origins remain unclear and require further investigation.

MSTE treatment significantly enhanced the SiV center emission intensity compared to air annealing and MSTE regardless of the initial doping level as can be seen in Fig. 4 a). Fig. 4 b) shows clear correlation between increasing silane concentration and enhanced SiV center emission intensity [3]. This relationship was particularly evident in PL spectra of MSTE-treated samples with varying silane concentrations, where the spectra were normalized at 738 nm to highlight the variations in SiV center intensity.

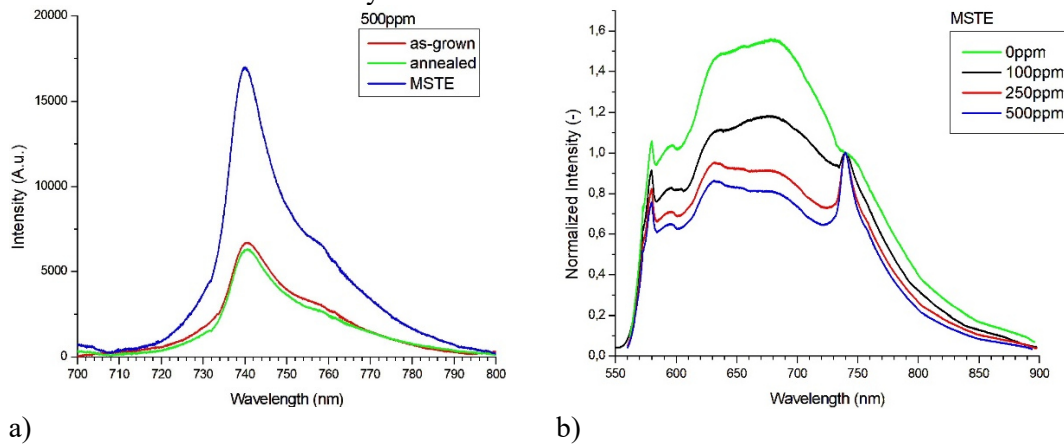


Fig. 4 Comparison of PL spectra a) for as-grown, annealed and MSTE-treated UNCD samples b) for different silane concentrations in the gas mixture after MSTE.

Conclusions

UNCD films containing SiV centers were successfully deposited using MWPECVD with varying silane concentrations. SEM analysis confirmed the synthesis and revealed morphological and thickness changes due to SiH₄ addition. Raman spectroscopy verified the UNCD character, while PL results demonstrated increasing SiV center content with higher silane concentrations. The MSTE process was employed to fabricate nanoparticles, resulting in selective etching of sp²-bonded carbon at grain boundaries. This approach proved more effective than control experiments using air or oxygen annealing.

The study highlights the potential of SiV-doped UNCD films for quantum applications. The MSTE process offers a promising method for creating nanoporous structures with enhanced surface effects.

References

- [1] Qi Sun et al. Surface structure and electric properties of nitrogen incorporated NCD films. doi: <https://doi.org/10.1016/j.vacuum.2016.12.040>.
- [2] Marcus W Doherty et al. The nitrogen-vacancy colour centre in diamond. In: *Physics Reports* 528.1 (2013), pp. 1–45.
- [3] Tímea Meřová. Preparation and characterisation of diamond optics structures.
- [4] František Trojánek et al. Light emission dynamics of silicon vacancy centers

in a polycrystalline diamond thin film. In: *Nanoscale* 15 (Jan. 2023). doi:
10.1039/d2nr05470a.

Acknowledgement

This work was supported by the Grant Agency of the Czech Technical University in Prague,
grant No. SGS22/182/OHK4/3T/14.

Preparation of protein single crystals for electron diffraction

Nastasja Viktorovna Samochvalova^{1,2}

¹Department of Solid State Physics, Faculty of Nuclear Sciences and Physical Engineering, Czech Technical University in Prague

²Laboratory of Structure and Function of Biomolecules, Institute of Biotechnology of Czech Academy of Sciences

Abstract

The use of electron crystallography in structural biology is gradually increasing due to the properties of electrons such as strong interaction with matter and negative charge. Using these properties, it is then easier to determine the position of ions than in X-ray structural analysis or to study crystals of very small dimensions. Procedures for the preparation of protein crystal samples for electron diffraction as well as the subsequent processing of diffraction data are gradually being standardized. This work deals with the preparation of microcrystals of two selected proteins, thaumatin and a bilirubin oxidase mutant, by changing already known crystallization conditions and the subsequent detection of these microcrystals using SONICC technology.

Keywords: Protein crystallography, electron structural analysis, crystal growth.

Introduction

Proteins are organic substances consisting of amino acids linked by a peptide bond. Knowledge of the structure of these biopolymers is very important and often crucial for understanding various biological processes, drug development and much more. Methods such as nuclear magnetic resonance, diffraction-based methods or the now emerging cryo-electron microscopy are used to study proteins. So far, X-ray diffraction analysis remains the most widely used diffraction method for protein structure determination.

In general, for the phenomenon of diffraction to occur, an object with a periodic arrangement, such as a crystal, is needed. Although there are exceptions, most proteins are not crystalline in nature. Finding the right conditions for protein crystal growth is often a time-consuming task. In addition, for X-ray diffraction, crystals need to be large enough, which some proteins simply do not form. Therefore, electron crystallography, which uses crystals with dimensions of several tens of micrometers, has also been developed in the last few years.

In addition, electron diffraction makes it easier to identify light atoms such as hydrogen and shows a higher sensitivity to charged groups. These properties are due to the strong Coulombic interaction of individual electrons with matter.

The first protein structure determined by Micro-ED method was the tetragonal chicken egg white lysozyme in 2013, followed by several other structures successfully determined previously by X-ray diffraction. More recently, Micro-ED was used to determine the structure of the metalloenzyme SaR2lox, which was previously unknown [2]. In this experiment, SaR2lox crystals were diffracted at a resolution of 3.0 Å. Although the Micro-ED method was originally developed for the structural study of biological substances, it could have a major impact on study methods in various fields of chemistry and drug development. It can provide high atomic resolution structures of complex and small molecules without much preparation of the sample itself.

Theory

0.1 X-ray and electron diffraction

X-rays are most commonly used for diffraction experiments, as their wavelength is comparable to the interatomic distance in a crystal. X-rays interact only with the electrons in the electron shell. For this reason, it is difficult to determine the exact position of the hydrogens from this method since they have only 1 electron. The depth of penetration of X-rays is determined by the intensity of the source and the material under investigation and can be up to several millimetres. The relationship between the intensity obtained by X-ray diffraction and the volume of the crystal is given by Darwin's relation:

$$I_{hkl} = I_0 r_e^2 \frac{V_{crystal}}{V} \frac{\lambda^3 L}{\omega V} P A |\mathbf{F}_{hkl}|^2, \quad (1)$$

where I_{hkl} is the measured intensity, I_0 is the intensity of the incident beam, r_e is the classical radius of the electron, $V_{crystal}$ is the volume of the whole crystal, and V is the volume of the ground cell, λ is the wavelength of the X-ray beam, L is the Lorentz factor, ω is the angular frequency, P is the polarization factor, A is the absorption factor, and \mathbf{F}_{hkl} is the structure factor.

As can also be seen from the relation (1), the problem of studying single crystals with X-rays arises when studying crystals with small volume. Electron diffraction therefore appears to be a potential alternative in the study of protein microcrystals.

Electrons interact strongly with matter because the interaction is not only with the electrons in the electron shell, but also with the nucleus [3]. This leads to a larger matter scattering cross section for electrons than for X-rays. High-energy electrons have shorter wavelengths (0.0251–0.0197 Å for 200–300 keV photons) than X-rays (1.0332 Å for 12 keV photons) [4].

Electrons also cause several orders of magnitude less damage than X-rays per elastic scattering, which is very important in the study of biological macromolecules.

0.2 Protein crystallization

Protein crystals are macromolecular crystals, therefore the search for crystallization conditions for protein crystal growth is an empirical and complex process. There is no theory that leads flawlessly to the desired results. Because of the complicated structure of protein molecules and the relatively weak interaction between individual protein molecules in solution per unit molecular surface area, the crystallization process is very sensitive to the physical and chemical conditions of the system [5]. In experiments using X-rays, the aim is to produce small numbers of large single crystals. For this purpose, it is important that the system has a small nucleation rate and gradually reaches the metastable zone. In the case of experiments using electrons, microcrystals are used and therefore the nucleation rate must be very high. For this purpose, additives can be added to the crystallization solutions to expand the nucleation zone of the protein in question [6].

Traditional crystallization methods such as the batch method, microcrystallization under oil or diffusion-based methods such as the sitting and hanging drop method can be modified to grow microcrystals. Moreover, due to the requirement for small crystals, non-standard methods such as in-cell crystallization or crystallization of proteins using liquid-liquid phase separation, which is typical only for some proteins, can also be used.

Results and Discussion

The proteins thaumatin and bilirubin oxidase were selected for experiments to optimize crystallization methods for targeted growth of protein microcrystals. Several crystallization methods such as the sitting and hanging drop method and the microcrystallization under oil were used to produce thaumatin crystals. To modify these conditions for the growth of micro- and nanocrystals, two approaches were used, namely changing in the concentrations of crystallization and protein solution or changing the ratio of the volumes of crystallization solution to protein solution. In the case of thaumatin, the hanging drop method was found to be the most suitable method for the preparation of microcrystals, where the ratio of the volumes of protein solution to crystallization solution was 8:10. In this experiment, the same initial crystallization condition was used in all drops: 20 % $\frac{w}{v}$ Potassium sodium tartrate tetrahydrate (NaKTart), 15 % $\frac{v}{v}$ ethylene glycol and 0.1 M BIS-TRIS at pH 6.6, and the same protein solution containing 50 mg · ml⁻¹ thaumatin and 275 mM Sodium acetate (NaAc). As can be seen in Fig.1 and Fig.2, microcrystals grew in the droplet at the given ratio. The formation of these microcrystals under these conditions could be monitored using the patented technology SONICC (Formulatrix).



Figure 1: Thaumatin microcrystals grown by the hanging drop method. Ratio of protein solution to crystallization condition 8:10. With a crystallization condition of 20 % $\frac{w}{v}$ NaKTart, 15 % $\frac{v}{v}$ ethylene glycol, 0.1 M BIS-TRIS at pH 6.6 and a protein solution of 50 mg · ml⁻¹ thaumatin and 275 mM NaAc. The line corresponds to 600 μm. (RI 1000)

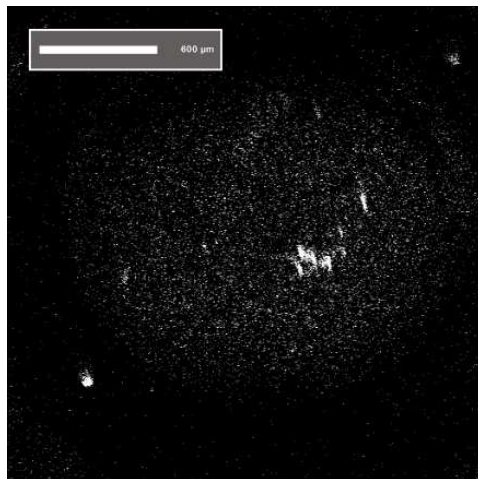


Figure 2: Image of the same droplet taken with SONICC technology in SHG mode, where visible particles correspond to protein microcrystals. The line segment corresponds to 600 μm. (RI 1000)

In the case of bilirubin oxidase, several functional variants were prepared for the purpose of the analysis of the role of the Trp396-His398 adduct. In the experiments described in this paper, one of these variants, more precisely MvBOxW396A, was worked with when Trp396 was mutated to alanine. This protein was prepared and described in detail in the work of Kovale et al. [7].



Figure 3: Crystals of MvBOxW396A, growth by the hanging drop method. Crystallization condition 0.09 M succinic acid, 14 % $\frac{w}{v}$ PEG 3350 and protein solution 25 mM Tris/HCl, pH 7.5 with 250 mM NaCl and 25 mg · ml⁻¹ MvBOxW396A. The line corresponds to 400 μm. (Olympus Stereomicroscope)

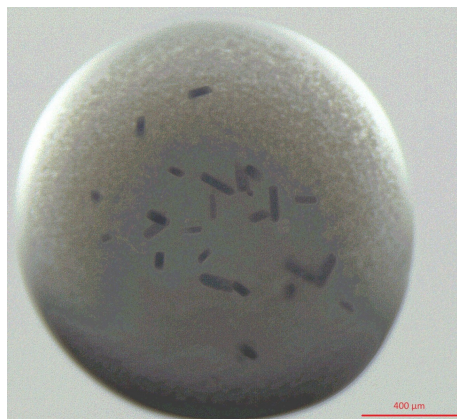


Figure 4: Crystals of MvBOxW396A, growth by the hanging drop method. Crystallization condition 0.1 M succinic acid, 16 % $\frac{w}{v}$ PEG 3350 and protein solution 25 mM Tris/HCl, pH 7.5 with 250 mM NaCl and 25 mg · ml⁻¹ MvBOxW396A. The line corresponds to 400 μm. (Olympus Stereomicroscope)

For crystallization were used known crystallization conditions from [7]. Under these conditions, characteristic blue crystals of bilirubin oxidase grew, suitable in size for X-ray diffraction. The crystallization condition contained 0.09 M succinic acid, 14 % $\frac{w}{v}$ PEG 3350 (see Fig.3) or 0.1 M succinic acid and 16 % $\frac{w}{v}$ PEG 3350 (see Fig.4).

The optimization of crystallization conditions for the formation of microcrystals was performed by changing the ratio of crystallization solution to protein solution. In these experiments, bilirubin oxidase crystals were of different sizes, but neither microcrystals nor nanocrystals were detected. Thus, microcrystals of the bilirubin oxidase mutant either did not form or there may have been a problem in the actual detection of possible micro- or nanocrystals, due to the fact that bilirubin oxidase crystals grow most often from the precipitate, which is still partially present after crystal growth and may noticeably attenuate the SHG or UV-TPEF signal when detected by SONICC technology. Thus, it can be said that the application of the techniques used in the case of this target molecule is more complicated and requires further development of procedures to achieve unambiguously detectable growth of micro- and nanocrystals even with a small amount of sample.

Conclusions

The aim of this work was the modification of the crystallisation conditions for the formation of detectable micro-crystals. For selected proteins thaumatin and bilirubin oxidase, crystallization conditions were successfully found and crystals were grown. For thaumatin, the conditions for microcrystal formation were also successfully found by varying the ratio of the volumes of crystallization solution to protein solution and by varying the concentrations of the two solutions. The best crystallization method with emphasis on microcrystal formation in the case of thaumatin was the hanging drop method, where the ratio of protein solution to crystallization solution was 8:10. In the case of bilirubin oxidase, crystallization conditions suitable for X-ray diffraction were found.

The droplets were observed using the patented SONICC technology and in some cases a signal was detected in the SHG mode. In the case of bilirubin oxidase, only crystals suitable for X-ray diffraction but too large for electron diffraction could be detected. For the time being, SONICC technology is an inseparable and very important part of the microcrystal preparation process, as modes such as SHG and UV-TPEF can be used to detect very small crystals that would not be visible with other techniques.

The diffraction properties of the obtained microcrystals were also verified in an electron microscope. Diffraction was not observed probably due to damage of the crystals during transfer to the grid.

It appears that sample preparation for this structural technique with small amounts of rare material is not yet fully resolved and requires further development and optimization. This may include the introduction of new procedures aimed at targeted formation of microcrystals and nanocrystals with the least possible sample consumption.

References

1. SAMOCHVALOVA, Nastasja. *Preparation of protein single crystals for electron diffraction*. 2024. Bachelor's thesis. Czech Technical University in Prague, Faculty of nuclear sciences a physical engineering, Department of Solid State Physics.
2. XU, Hongyi (Justin); LEBRETTE, Hugo; CLABBERS, Max; ZHAO, Jingjing; GRIESE, Julia; ZOU, Xiaodong; HÖGBOM, Martin. Solving a new R2lox protein structure by microcrystal electron diffraction. *Science Advances*. 2019, roč. 5, eaax4621. Available from DOI: 10.1126/sciadv.aax4621.
3. PALATINUS L. a Kratochvíl, B. Elektronová difrakce – nový nástroj pro řešení krystalové struktury látek [Electron Diffraction – New Tool for Crystal Structure Solutions]. *Chemické listy*. 2021, 368–374.
4. CLABBERS, Max; XU, Hongyi (Justin). Macromolecular crystallography using microcrystal electron diffraction. *Acta Crystallographica Section D Structural Biology*. 2021, roč. 77. Available from DOI: 10.1107/S2059798320016368.
5. VEKILOV, Peter; CHERNOV, Alexander. The Physics of Protein Crystallization. *Solid State Physics*. 2002, roč. 57. ISBN 9780126077575. Available from DOI: 10.1016/S0081-1947(08)60179-4.

6. FAHIM, Aisha; PHAM, Jenny; THOMAS, Shamberia; ANNUNZIATA, Onofrio. Boosting protein crystallization from liquid-liquid phase separation by increasing metastability gap. *Journal of Molecular Liquids*. 2024, roč. 398, p. 124164. Available from DOI: 10.1016/j.molliq.2024.124164.
7. KOVAŘ, Tomáš; SVECOVA, Leona; ØSTERGAARD, Lars; DUSKOVA, Jarmila; HAŠEK, Jindřich; KOLENKO, Petr; FEJFAROVÁ, Karla; STRÁNSKÝ, Jan; TRUNDOVA, Maria; DOHNALEK, Jan. Trp–His covalent adduct in bilirubin oxidase is crucial for effective bilirubin binding but has a minor role in electron transfer. *Scientific Reports*. 2019, roč. 9, p. 13700. Available from DOI: 10.1038/s41598-019-50105-3.

Acknowledgement

This work was supported by the Grant Agency of the Czech Technical University in Prague, grant No. SGS13/219/OHK4/3T/14, and Czech Science Foundation, grant No. 14-36566G, and institutional support from Biotechnology institute AV CR, v. v. i. RVO: 86652036. Also I would like to thank Mgr. Tereza Skálová, Ph.D from Laboratory of structure and function of biomolecules for help in preparing samples for the electron microscope.

Preparation of High-temperature YBCO Superconductors Thin Films Using Ionized Jet Deposition

Michal Jůza, Jakub Skočdopole

Department of Solid State Engineering, Faculty of Nuclear Sciences and Physical
Engineering, Czech Technical University in Prague
juzamich@cvut.cz

Abstract

Construction of future cities will require optimization of mass-production of economically achievable High-temperature superconductors. Ionized Jet Deposition has a potential to overcome the current limitations. We used this method to prepare 11 samples of YBCO superconductor thin films in 2 series scanning the differences in substrate material and substrate temperature. Analysis of film thickness showed strong dependence of growth speed on the deposition pressure. The thickness of the samples ranged between 600 nm and 1400 nm. After annealing and oxidation process qualitative phase analysis showed presence of superconducting phase $\text{YBa}_2\text{Cu}_3\text{O}_{7-x}$ on all of the samples. Analysis of electrical properties proved superconducting properties of the selected annealed samples with T_C ranging from 70 K to 85 K.

Keywords: High-temperature superconductors; YBCO; Thin films; Ionized jet deposition

Introduction

Could application of superconductive materials be the next huge step up for humanity? That progress relies on the optimization of mass-production of High-temperature superconductors (HTS) with sufficient properties, that is both scalable and economically achievable. Ceramic high temperature superconductors seem to be a appropriate type of material for that purpose. They are usually very fragile and not as easy to manufacture as metal conductors. The use of thin film deposition is therefore a necessity for their usage in power transmission.

The conventional state of the art methods for preparation of HTS thin films are Pulsed laser deposition and Magnetron sputtering. Recently, Ionized Jet Deposition (IJD) is getting attraction for its simplicity and potential in industrial applications.

IJD relies on strong electron pulse induced by high voltage primary source in an evacuated chamber. This electron pulse ablates the target material, which is then deposited on the surface of the substrate and thus creates thin film of that material. The process can be controlled by different deposition gasses and different accelerator voltage

However, the deposition of high-quality YBCO films relies strongly on the correct deposition parameters. Especially on the surface temperature during the deposition as well as during later annealing process. The another important variable is deposition pressure, which strongly influence the thickness and roughness of the layer. It is also important to obey the correct stoichiometry of the deposited layer, in order to be superconductive. Nevertheless, using IJD it is possible to overcome these challenges and create superconducting thin-films with sufficient quality and properties.

Materials & Methods

YBCO material and properties

High-temperature superconductors based on YBaCuO structure are ceramic materials. The structure is shown at figure 1a. However, YBCO is difficult to manufacture as bulk material and the process of crystalization is very slow and energetically demanding. In order to achieve economical approach to manufacture large amount of superconducting wires and cables, one need to utilize some form of thin films deposition method. Our method of choice was Ionized jet deposition, the novel thin film deposition method, with huge industrial potential. The creation of correct phase is a challenge, because of correct stoichiometry. The phase diagram of the system is shown at fig. 1b. There the superconducting phase is denoted as "123".

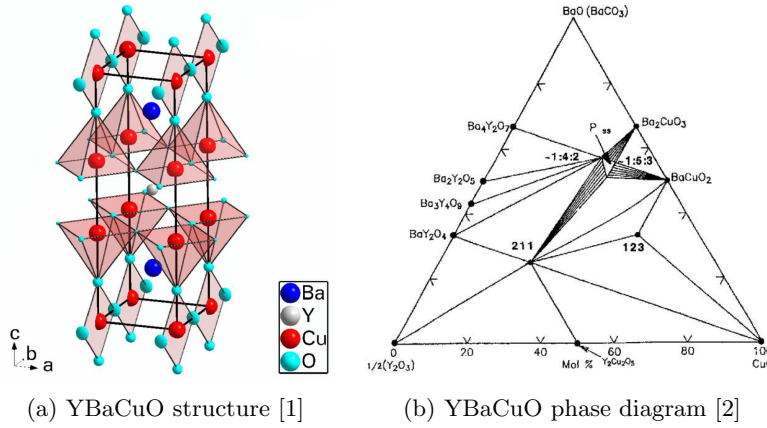


Figure 1: YBaCuO system

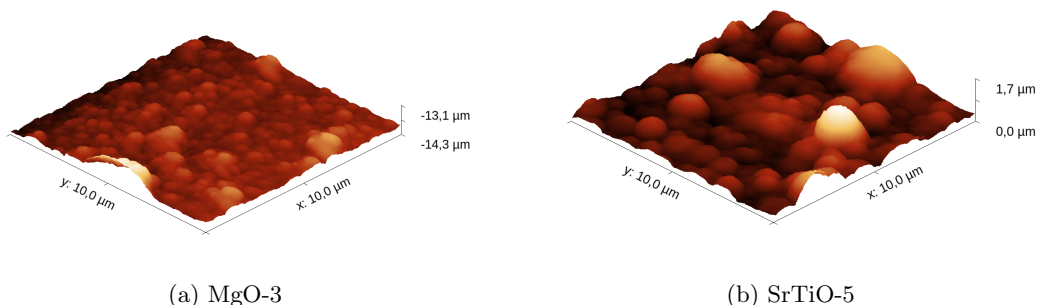
Experimental

Experimental setup

All depositions were performed using the JetDep100 apparatus at the Department of Solid State Engineering at FNSPE CTU in Prague. We created 11 samples in 2 series. The difference between these series was in the used substrate material. For the first series we choose MgO single crystal and for second series the substrate was SrTiO₃ single crystal. These material are mostly used for thin film epitaxial growth of YBCO superconductor, due to their good lattice constants match. For all deposition we used sintered YBa₂Cu₃O_{7-x} target manufactured by company CAN Superconductors [3]. Deposition gas wor pure oxygen (purity 4.5). IJD voltage was set to 17 kV with frequency of 15 Hz. Target-substrate distance was 110 mm.

For the MgO series we have choosen based on the previous research [4] the deposition substrate temperature between 480 °C and 530 °C with steps of 10 °C. The deposition time was 30 minutes. For the SrTiO series, we have choose, based on the results of MgO series, narrower temperature interval between 495 °C and 515 °C with steps of 5 °C. The

Figure 2: Surface morphology obtained from Atomic force microscopy



deposition time was extended to 45 minutes to make the samples thicker. The substrate temperature and pressure (initial and deposition) for each sample is listed in table 1

Table 1: Deposition parameters for MgO and SrTiO series respectively

Sample	MgO-1	MgO-2	MgO-3	MgO-4	MgO-5	MgO-6
substrate temp. [°C]	480	490	500	510	520	530
init. pressure [10^{-4} mbar]	0,7	1,0	0,6	0,8	0,7	0,7
dep. pressure [10^{-4} mbar]	5,4	5,4	5,4	5,0	4,4	4,0
Sample	SrTiO-1	SrTiO-2	SrTiO-3	SrTiO-4	SrTiO-5	
substrate temp. [°C]	515	510	505	500	495	
init. pressure [10^{-4} mbar]	0,6	0,6	0,7	0,6	0,6	
dep. pressure [10^{-4} mbar]	3,3	3,3	3,3	3,3	3,3	

After all analysis the samples were annealed at 900 °C for 3 hours in ambient atmosphere and then oxidated for 24 hours at 400 °C in oxygen atmosphere.

Results

We used Atomic force microscope Litescope AFM from company NenoVision using Akiyama probe on Department of solid state engineering (DSSE) on FNSPE CTU in Prague. For qualitative phase analysis we used X-ray diffractometer Empyrean from PANalytical on DSSE using Co X-ray tube ($\lambda(CoK_{\alpha 1}) = 0,1789$ nm) in Bragg-Brentano configuration. For electrical properties Electrical Transport Option (ETO) module in Physical Property Measurement System (PPMS) device from company Quantum Design on FZU CAS. [6] We measured layer thickness and surface morphology using Atomic layer deposition

In table 2 there are listed thickness of the samples in each series respectively. This value was determined using the Gwiddion open source software [5]. In the next table 3 and 4 are listed found phases on both pre-annealed and post-annealed samples determined using XRD.

Figure 3: XRD of the sample SrTiO-3

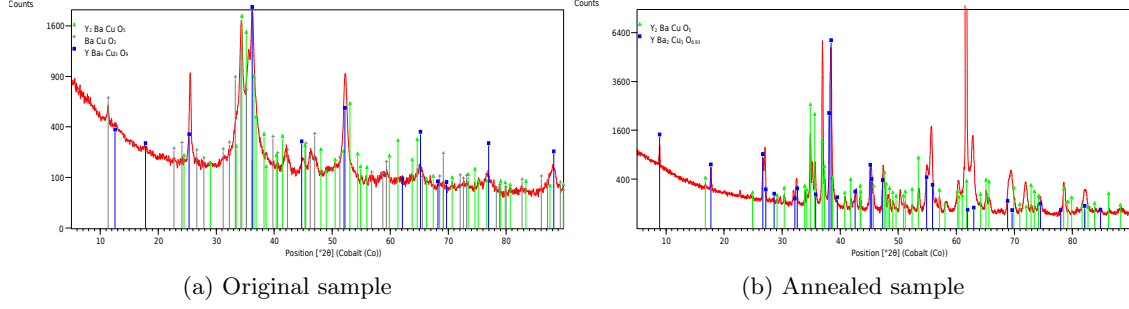


Table 2: Sample thickness for MgO and SrTiO series respectively, where t_S is substrate temperature, p_d deposition pressure and d layer thickness.

Sample	MgO-1	MgO-2	MgO-3	MgO-4	MgO-5	MgO-6
t_S [°C]	480	490	500	510	520	530
p_d [10^{-4} mbar]	5, 4	5, 4	5, 4	5, 0	4, 4	4, 0
d [nm]	720 ± 80	700 ± 50	600 ± 30	710 ± 30	1100 ± 20	940 ± 80

Sample	SrTiO-1	SrTiO-2	SrTiO-3	SrTiO-4	SrTiO-5
t_S [°C]	515	510	505	500	495
p_d [10^{-4} mbar]	3, 3	3, 3	3, 3	3, 3	3, 3
d [nm]	1000 ± 160	1480 ± 100	1100 ± 60	1030 ± 60	880 ± 70

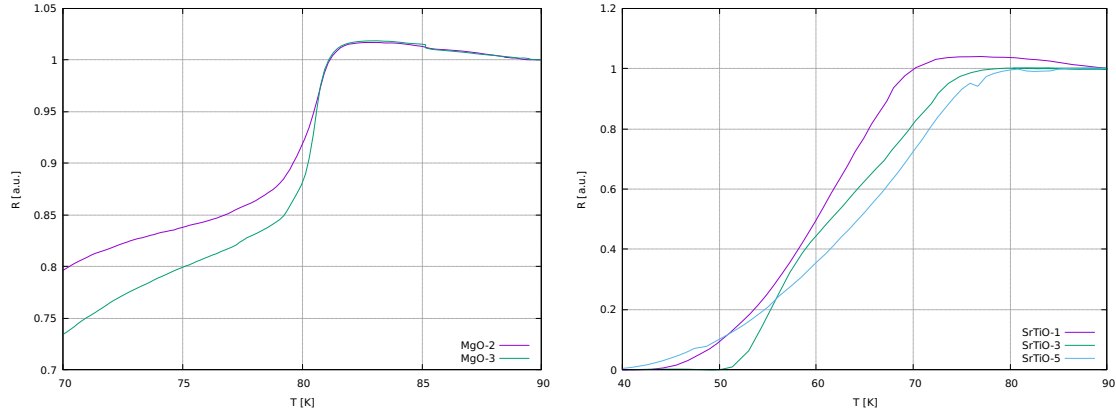
Table 3: Phase analysis of MgO series, where t_S [°C] is the substrate temperature.

Sample	t_S	phase composition pre annealing	phase composition past annealing
MgO-1	480	Y_2BaCuO_5 , $BaCu_2O_2$, Y_2O_3	$YBa_2Cu_3O_{7-x}$, $Ba_4Y_2O_7$
MgO-2	490	Y_2BaCuO_5 , $BaCu_2O_2$, BaO_2 , Y_2O_3	$YBa_2Cu_3O_{7-x}$
MgO-3	500	Y_2BaCuO_5 , $BaCuO_2$, $YBa_2Cu_3O_{7-x}$, BaO_2	$YBa_2Cu_3O_{7-x}$, BaY_2O_4
MgO-4	510	Y_2BaCuO_5 , $BaCu_2O_2$, $YBa_2Cu_3O_{7-x}$, BaO_2	$YBa_2Cu_3O_{7-x}$, Y_2O_3
MgO-5	520	Y_2BaCuO_5 , $BaCu_2O_2$, $BaCO_3$, BaO_2 , Y_2O_3	$YBa_2Cu_3O_{7-x}$, $BaCu_3O_4$
MgO-6	530	Y_2BaCuO_5 , $BaCu_2O_2$	$YBa_2Cu_3O_{7-x}$, $BaCuO_2$, Cu_2O

Table 4: Phase analysis of SrTiO series, where t_S [°C] is the substrate temperature.

Sample	t_S	phase composition pre annealing	phase composition past annealing
SrTiO-1	515	$YBa_4Cu_3O_9$, Y_2O_3	$YBa_2Cu_3O_{7-x}$, Y_2BaCuO_5
SrTiO-2	510	$YBa_4Cu_3O_9$, $YCuO_2$	$YBa_2Cu_3O_{7-x}$, Y_2BaCuO_5
SrTiO-3	505	$YBa_4Cu_3O_9$, Y_2BaCuO_5 , $BaCuO_2$	$YBa_2Cu_3O_{7-x}$, Y_2BaCuO_5
SrTiO-4	500	$YBa_4Cu_3O_9$, Y_2BaCuO_5 , $BaCuO_2$	$YBa_2Cu_3O_{7-x}$, Y_2BaCuO_5
SrTiO-5	495	$YBa_4Cu_3O_9$, Y_2BaCuO_5 , $BaCuO_2$	$YBa_2Cu_3O_{7-x}$, Y_2BaCuO_5

Figure 4: Dependence of the resistance on temperature for choosen annealed samples from MgO and SrTiO series.



Discussion

The thickness analysis showed strong dependence on the deposition pressure for MgO series. With decrease of the deposition pressure the thickness increases. With lower pressure there is a stronger electron pulse and the thermal sputtering is inhibited in behalf of ablation. The differences of sample thickness in SrTiO series could be cause by different position of the target towards IJD head.

XRD showed significant differences in phase composition between different samples in MgO series. Sample MgO-1 contains "green phase" Y_2BaCuO_5 for the most part. Sample MgO-2 is similar in terms of qualitative phase composition. Most significant phase change occurs at the substrate temperature of 500 °C for the sample MgO-3, where XRD revealed presence of superconducting phase $YBa_2Cu_3O_{7-x}$. Similar composition but with less evidence of superconducting phase showed also sample MgO-4. In sample MgO-5 $BaCO_3$ appears, which could be caused by high temperature of 520 °C. For sample MgO-6 prepared at 530 °C the phase composition is very different. From phase analysis of MgO series the optimal temperature interval lays between 500 °C and 510 °C.

Based on analysis of previous series the second series was prepared using narrower temperature interval between 495 °C and 515 °C with smaller step of 5 °C. $SrTiO_3$ should have better lattice constants match than MgO so it should be more appropriate for YBCO superconductor epitaxial growth. In case of SrTiO series the phase composition was more consistent. For all of the samples of SrTiO series there was found $YBa_4Cu_3O_9$ (143) phase. First 2 samples of the series do not contain any other 4-element phase, which indicates, that temperature above 510 °C is too high. Sample SrTiO-3 prepared at 505 °C contains the greatest amount of 143 and even more the phase Y_2BaCuO_5 is also present. Last two samples have similar composition to sample SrTiO-3 but with less amount of 143 phase.

After annealing phase analysis uncovered presence of the superconducting phase $YBa_2Cu_3O_{7-x}$ for all samples. In the series there were many other phases present with strong peaks from the substrate due to its smaller thickness in comparison with SrTiO series. In the samples of SrTiO series the superconducting phase was present always at high quantity. From XRD there is no significant evidence of the texture of the layers.

Measurement of the electrical properties of the choiced annealed samples of MgO series

showed steep decrease of the electrical resistance at temperature of about 80 K. For annealed samples from SrTiO series the T_C is around 75 K with complete loss of electrical resistance at temperatures between 40 K and 50 K. The decrease is, however not too steep, which is probably caused by not sufficient oxidation of the samples, which influence T_C .

Conclusion

In this research we focused on the preparation and analysis of thin films of high-temperature superconductors base on YBCO using Ionized jet deposition. We have prepared 11 samples in total in two series which differed in substrate material, MgO and SrTiO₃ single crystal.

The thickness analysis showed strong dependence of the growth speed on the deposition pressure. With the decrease of the pressure the thickness increases. XRD showed that optimal deposition temperature for YBCO lies between 500 °C and 505 °C, which corresponds with theory. XRP also proved that SrTiO₃ substrate is more appropriate for preparation of YBCO superconductors. However, the superconducting phase still do not grow during the deposition, this still needs to be done in annealing process after deposition. All annealed samples contained superconducting phase in great amount.

At selected annealed samples from both series the electrical properties were measured which also proved the superconducting character of prepared samples with T_C between 70 K and 85 K.

References

- [1] T. Košťál *Příprava a rentgenová difrakční analýza supravodivých tenkých vrstev nanosených metodou IJD* Bachelor thesis, FNSPE CTU in Prague, 2021
- [2] J. Skočdopole *Investigation of Functional Thin Films Prepared by Ionized Jet Deposition Method* Ph.D. thesis, FNSPE CTU in Prague, 2023
- [3] CAN Superconductors. URL: <https://www.can-superconductors.com>
- [4] M. Jůza. *Optimization of IJD deposition parameters of high temperature superconductors thin films based on YBCO*. Bachelor thesis, FNSPE CTU in Prague, 2022.
- [5] *Gwyddion - Free SPM analysis software* URL: <http://gwyddion.net>
- [6] M. Jůza. *Study of the influence of deposition parameters on properties of thin films of high-temperature superconductors prepared by IJD method* Diploma thesis, FNSPE CTU in Prague, 2024

Acknowledgment

This work was supported by the Grant Agency of the Czech Technical University in Prague, grant No. SGS22/183/OHK4/3T/14.

Preparation and analysis of plasmonic Ag thin films deposited by Ionized Jet Deposition method and Magnetron Sputtering method

Jáchym Lis^{1,2}

¹Department of Solid State Engineering, Faculty of Nuclear Sciences and Physical Engineering, Czech Technical University in Prague

²Institute of Physics of the Czech Academy of Sciences
lisjachy@cvut.cz

Abstract

Plasmonics is an advanced technology in the field of optical sensors. A methodology for the preparation of silver thin films suitable for plasmonics by Ionized Jet Deposition is developed. The RF Magnetron sputtering method is used for comparison as a well mastered technique. The roughness, relative permittivity and growth rate of the layers are analyzed using atomic force microscopy, attenuated total reflection and ellipsometry methods. Samples prepared by Magnetron Sputtering show slightly better properties, but the preparation by Ionized Jet Deposition can be further optimized.

Keywords: Surface Plasmonic Resonation; Ionized Jet Deposition; Magnetron Sputtering; thin films.

Introduction

In the past two decades, plasmonic has progressed to a mature technology allowing the manipulation of light in various applications, including sensorics. Plasmonic oscillations are oscillations of free electron gas in metals, which strongly influence the optical properties (reflectancy and transmittancy) of thin metal layers. Plasmonic sensors offer a versatile state-of-the-art optical sensors which can be used for example as distributed gas sensors.

As plasmonic properties rely on free electron gas, the elements from I.B. group - Cu, Ag, Au - whose metal phases exhibit high free electron concentrations, play an important role in plasmonic structures. It is necessary to investigate the manufacturing of plasmonic Ag layers, which are often used as a base layer in plasmonic multilayer structures in sensorics due to Ag's superior plasmonic properties.

Ionized jet deposition method (IJD) is a novel method belonging to the group of physical vapor deposition (PVD) techniques. The method is based on generating short pulses of electrons with energies between 5 – 20 kV, which ablate the target material in an evacuated chamber. The plasma plume of the target material then travels across the chamber towards the substrate and forms the thin film. Due to its simplicity and relatively low operating expenses, the IJD method is a good candidate for upscaling and industrial use of thin films deposition.

In order to have good surface plasmon resonance properties the films need to have very smooth and consistent surface and have consistent low thickness (in the order of tens nm). We investigated the manufacturing of plasmonic Ag thin films using the IJD method and optimised deposition parameters to create films with desired thickness and

surface properties. We compared our samples with plasmonic Ag layers manufactured using the well established Magnetron sputtering (MS) method.

Materials and Methods

Substrate, deposition material. Common laboratory glass and fused silica were used as substrates. Pure Ag targets were used for the deposition of thin Ag films. TODO: pŭvod materiálu

Ionized Jet Deposition. The IJD deposition system JetDep 100 (manufactured by Noivion s. r. o. and Czech Vacuum s. r. o., Czech Republic) was used in the preparation of thin Ag films. The IJD deposition parameters common for all prepared samples were as follows: The pulse frequency was set to 100 Hz, the distance between substrate and target was set to 110 mm, the distance between the IJD head and target was set to 3 mm. The mean primary electron beam spot diameter amounted to 1 mm on the target. The substrate temperature was set to 300 K. A gas mixture of Ar+6 vol. % H₂ was used as the IJD working gas (purity 99.999%, provided by Linde Technoplyn, s.r.o., Czech Republic). The initial pressure before deposition and the working pressure were set in the range of $(3, 0 - 4, 1) \times 10^{-3}$ Pa and $(5, 2 - 7, 2) \times 10^{-2}$ Pa, respectively. The deposition voltage was varied between 9 – 12 kV and deposition time between 20 – 60 min. Microscope slides were used as substrates.

Magnetron Sputtering. The control samples of thin Ag films were prepared using magnetron sputtering system installed in the Institute of Physics, Czech Academy of Sciences. The power of RF source was set to 100 W, the sputtering target was water-cooled and substrate was at a room temperature. The working pressure was set to 1 Pa, Ar was used as the working gas. In two cases, a predeposition of AgO_x were performed by using a mixture of Ar and O in the ratio of 2 : 1. The gases were of purity 99.999%, provided by Linde Technoplyn, s.r.o., Czech Republic. Microscope slides and fused silica were used as substrates.

Sample analysis. The root mean square (RMS) roughness of both sample series were analyzed using Atomic Force Microscopy (LiuteScope equipped with the Akyiama probe, manufactured by NenoVision s. r. o.). The thickness, relative permittivity and EMA Roughness (calculated according to Bruggeman model of effective media approximation[1]) were analyzed using Attenuated Total Reflection method in the Kretschmann configuration (laser $\lambda = 632,8$ nm, BK7 prism and photodiode detector) and Ellipsometry method (M-2000X manufactured by J. A. Woollam Co., Inc).

The AFM data were analyzed using the Gwyddion¹ software in version 2.61 in order to evaluate the RMS roughness of the samples. The ATR data were processed using the tmm Python package² in version 0.1.8 in order to evaluate the surface plasmon properties of the prepared films and calculate thickness, EMA roughness and relative permittivity. The ellipsometry data analysis was performed using the CompleteEASE software in version 6.56 in order to evaluate the surface plasmon properties of the prepared films and calculate thickness, EMA roughness and relative permittivity.

¹<http://gwyddion.net/>

²<https://pypi.org/project/tmm/>

Results and Discussion

Roughness

Using magnetron sputtering method, a lower roughness was achieved, which is essential factor for excitation of surface plasmon-polariton. The lower roughness was achieved mainly by switching to fused silica substrates and short (2 s) predeposition of AgO_x , because it nucleates on the substrate by layers and Ag nucleates on it by layers, while Ag on the substrate nucleates by island [2], so probably a similar improvement is possible in the IJD method.

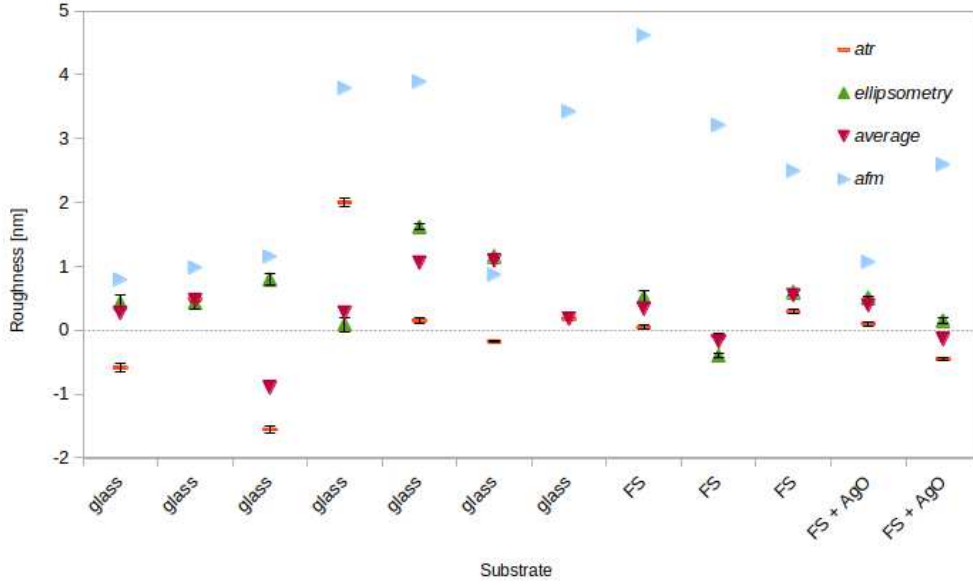


Figure 1: Magnetron sputtering series: Roughness on different substrates

Relative permittivity

At $\lambda = 632,8 \text{ nm}$, the relative permittivity achieved was close to relative permittivity of bulk Ag $(-18,281 + 0,48108i)^3$, which indicates purity and low porosity of thin Ag films. The average relative permittivity of the IJD series was $(-13,44 \pm 0,02) + (0,960 \pm 0,004)i$ on microscope slides. The Magnetron Sputtering series achieved $(-17,17 \pm 0,03) + (0,716 \pm 0,007)i$ on microscope slides, $(-16,74 \pm 0,03) + (0,840 \pm 0,009)i$ on fused silica and $(-15,50 \pm 0,02) + (0,886 \pm 0,009)i$ on fused silica with AgO_x predeposition. According to literature [2], the AgO_x should reduce to pure Ag during the deposition, but the relative permittivity value achieved suggests that it might not happen fully. The relative permittivity values of Magnetron Sputtering series compared to IJD series suggests that the Magnetron Sputtering method achieves better quality films (e. g. due to lower porosity).

³<https://refractiveindex.info/>

Growth rate

The average film growth rate using the IJD method was $(16,33 \pm 0,02)$ pm/s, increasing with the deposition voltage as expected. The average film growth rate using the Magnetron Sputtering method was $(1,1673 \pm 0,0004)$ nm/s, which is cca $60\times$ faster than the IJD method, but the deposition process is so fast it starts to be a problem to precisely control the thickness of the samples by manipulating the deposition time, while the IJD method being slower on the other hand offers better thickness control. The IJD deposition rate can be increased by increasing the deposition voltage, but it would probably also increase the roughness, thus decrease the quality of the samples.

Conclusions

At this time, the Magnetron Sputtering method offers better Ag thin films plasmonic properties, but it is better established method than the IJD method and the Ag deposition process is well optimized, so it is possible that by further development and optimization of the IJD deposition process we could achieve similar results. The further research should focus on deposition using the IJD method and fused silica as a substrate, alternatively also with the AgO_x predeposition, in order to decrease roughness and increasing the deposition voltage in order to increase growth rate.

References

- [1] D. A. G. Bruggeman. Berechnung verschiedener physikalischer Konstanten von heterogenen Substanzen. I. Dielektrizitätskonstanten und Leitfähigkeiten der Mischkörper aus isotropen Substanzen. *Annalen der Physik*. 1935; **416**(7):636-64. Available from: <https://onlinelibrary.wiley.com/doi/abs/10.1002/andp.19354160705>.
- [2] J. Bulř, M. Novotný, A. Lynnykova and J. Lančok. Preparation of nanostructured ultrathin silver layer. *Journal of Nanophotonics*. 2011; **5**(1):051511. Available from: <https://doi.org/10.1117/1.3562568>.

MOVPE grown AlGa_N layers on sapphire substrates for UV applications

Jan Batysta^{1,2}, Alice Hospodková², František Hájek^{2,3}, Jiří Pangrác², Karla Kuldová²,
Tomáš Hubáček²

¹Department of Solid State Engineering,
Faculty of Nuclear Sciences and Physical Engineering, Czech Technical University in Prague
²Department of semiconductors, Institute of Physics, Czech Academy of Sciences

Abstract

UV emitters without mercury are desired for many applications from photochemistry, agriculture to spectroscopic light sources. LEDs provide many benefits over standard mercury lamps. The group III-nitrides are promising material that can be tuned to large spectrum of emitting wavelengths and there are already commercially available devices for sale. Even though the material group is very successful, there is still room to make the LEDs more efficient.

Key words: MOCVD; UV emitters; III-group nitrides.

Introduction

The first breakthrough in III-group nitrides was the pioneering work of Akasaki, Amato and Nakamura who managed to overcome many technical challenges connected with preparation of a wide-bandgap semiconductor (GaN) with high crystalline quality which, as they demonstrated, could be successfully (though not trivially) grown to achieve electron and hole conductivity and efficient light emission. They were awarded the Nobel prize in physics in 2014 for their efforts [1]. This material is gallium nitride, with bandgap of 3,4 eV. This breakthrough started a small revolution in the way we produce white light using the first bright blue LED. Discovering the techniques of producing the III-group-nitride semiconductors (GaN, AlN, InN and alloys) lead to multiple new application areas. In this work we will focus on light sources beyond the blue LED into the ultraviolet region. This can be achieved by AlGa_N alloy, as the bandgap of such alloy spans region from 3,4 eV to 6,2 eV corresponding to wavelengths down to 200 nm in the deep ultraviolet (DUV) region. We will discuss the technology of MOVPE and results of experimental preparation of AlGa_N layer on sapphire. The basic properties of III-nitrides can be found in many publications, for example [2], [3], [4].

Technological overview

In this study we will discuss the preparation of AlGa_N layers on sapphire substrate. We prepare our samples via **metalorganic vapour-phase epitaxy** (MOVPE, alternatively known as metalorganic chemical vapour deposition: MOCVD). This is not the only possible source of UV light, or not the only source of preparation of III-group nitride epitaxial layers. For example, the Molecular Beam Epitaxy (MBE) is a major competitor in research, but for industry usage this technology is impractical.

Epitaxy by itself works by delivering atoms of desired material on a crystalline substrate, where the new material crystallises in the same crystalline structure as the underlying substrate. In MOVPE the atoms are sourced from chemical precursors: metalorganics. These are stable until

heated, after heating the molecules decompose into sources of single atomic elements carried onto the substrate. This process uses regulated pressures, usually between 50-1000 kPa, as in our apparatus. The pressure and a laminar flow are maintained by a vacuum pump and a butterfly valve. The substrate can be heated by radiofrequency (RF) or resistive heaters. The process temperature may vary from 700 to 1400 °C depending on desired growth of the structure. Typically, structures containing indium are grown at lower temperatures, while structures containing aluminium are grown at higher temperatures. The type of heating element does play a role in the epitaxial process. For some type of growths fast switching between growth temperatures is desirable. For this the RF heater is superior, but for more precise control over temperature distribution, resistive heater with more coils can perform better. That is especially needed for large substrate wafers.

The samples manufactured in for the purpose of this research were made in AIX 200 RF/S. This is a horizontal-type reactor with radiofrequency heater and with option of high temperature setup with susceptor made from TaC. With this setup the temperature can be over 1400 °C. The standard susceptors for lower temperature up to 1200 °C are made from SiC. A pyro detector is mounted bellow the susceptor measuring the so-called process temperature. Another pyro detector is mounted from the top as a part of in situ measurements by Laytec, which measure also wafer curvature and reflectance during the deposition process. The pyro detectors are used with an Eurotherm unit to provide stable temperature, because change of growth parameters inside the reactor affects the cooling of the wafer.

The term horizontal reactor describes which way the precursors and carrier gasses flow towards the substrate. Nonreactive gases are used as carrying gases, our machine can use hydrogen and nitrogen but theoretically any inert gas could be used. It is suggested in [3] that while horizontal reactors have better homogeneity, vertical (close-coupled showerhead) have better precursor yield. In our own experiments similar results are obtained in terms of growth to consumption ratio, the case of homogeneity is harder to discuss due to different heating elements and geometry of the reactors used in our laboratory.

Important aspect is also the choice of precursors. For the III-group, the usual precursors are three methyl or ethyl groups bonded to the metal atom. These molecules are known as metalorganics. Some precursors perform better in lower temperatures, some in higher. Based on previous experiences, trimethylgallium and trimethylaluminum were used in experiments discussed below. Ammonia serves as the nitrogen precursor. The precursors are sources of contaminants, mainly carbon and hydrogen.

Experimental

The first stage of the research is finding the right process to achieve suitable buffer for the active region. The goal is growing high quality AlGa_N on sapphire substrate, which is a nontrivial task. Even harder when we try to achieve a sufficiently high Al mole fraction, low density of threading dislocations and a flat surface. When growing any nitride on sapphire, it is necessary to make a nucleation layer that is a binary compound, GaN or AlN. For growing AlGa_N with smaller Al fraction around 25 percent it is better to use GaN as the nucleation layer, but one must be cautious because if we make the underlying GaN too thick, the AlGa_N layers on top will start cracking very soon due to the emerging tensile strain [5], [6], [7].

We have manufactured a series of AlGa_N layers with the goal of a smooth surface and low Threading Dislocation Density (TDD). The growth process has many parameters which were varied during the growths. We first started by growing AlGa_N directly on top of the GaN nucleation layer. The experiment were inspired by [8], but we soon switched to having a short five minute coalescence with GaN (without aluminium precursor). This led to improvements in surface

quality in form of emergence of c-plane facets. The emergence of holes in the surface of next batch of samples was successfully overgrown with higher growth rate and longer growth times. The set of main parameters can be seen in Table 1.

The quality of the surface can be assessed in Figure 2. In the end we managed to get a relatively smooth surface with sample 8 and 11. But still there can be seen some large irregularities with circular shape. These circles are flat and appear smooth on SEM (Scanning electron microscopy), but to assess the height difference of the circular mesas, we had one AFM (Atomic Force Microscopy) measured and the results can be seen in picture Figure 1.

Table 1 The main growth parameters used in the recipes for AlGaIn samples. First two samples were done without the GaN coalescence. In some parameters there was a gradual change across a period of time. This is outlined by having the final value set to be changed in a given amount of second. For example, 1700 in 2700 would mean the value was gradually changed to reach 1700 in 2700 seconds.

Param.	Nucleation				Coalescence GaN					Coalescence AlGaIn				
	time [s]	NH3 [sccm]	TMGa [sccm]	pressure [mBar]	time [s]	NH3 [sccm]	TMGa [sccm]	pressure [mBar]	temp [°C]	time [s]	NH3 [sccm]	AlGaIn [sccm]	pressure [mBar]	temp [°C]
1	180	1200	18	600	x	x	x	x	1120	3600	2700	25/25	50	1260 in 2400
2	180	1200	18	600	X	x	x	x	1100	3600	1700 to 2700	25/25	50	1260 in 2400
3	240	1200	18	600	300	1700	25	100 in 120	1100	3000	1700 to 2700	25/25	100	1260 in 2400
4	240	1200	18	600	300	1700	25	100 in 120	1100	3000	1700 to 2700	25/25	50	1260 in 2400
5	240	3000	36	600	300	1700	25	100 in 120	1100	3000	1700 to 2700	25/25	50	1260 in 2400
6	240	1200	18	600	300	1700	25	100 in 120	1100	3000	2700 to 3200	25/25	50	1260 in 2400
7	240	3000	36	600	300	2700	25	100	1100	7200	2700 to 3200	25/25	50	1260 in 2400
8	240	3000	36	600	300	3500	50	100	1100	7200	3500 to 4000	50/50	50	1260 in 2400
9	240	1200	18	600	300	1700	50	100	1100	5400	4000 in 1600	50/50	100	1260 in 1600
10	240	3000	30	600	300	2700	50	100	1100	3600	3500 in 2400	50/50	50	1260 in 3600

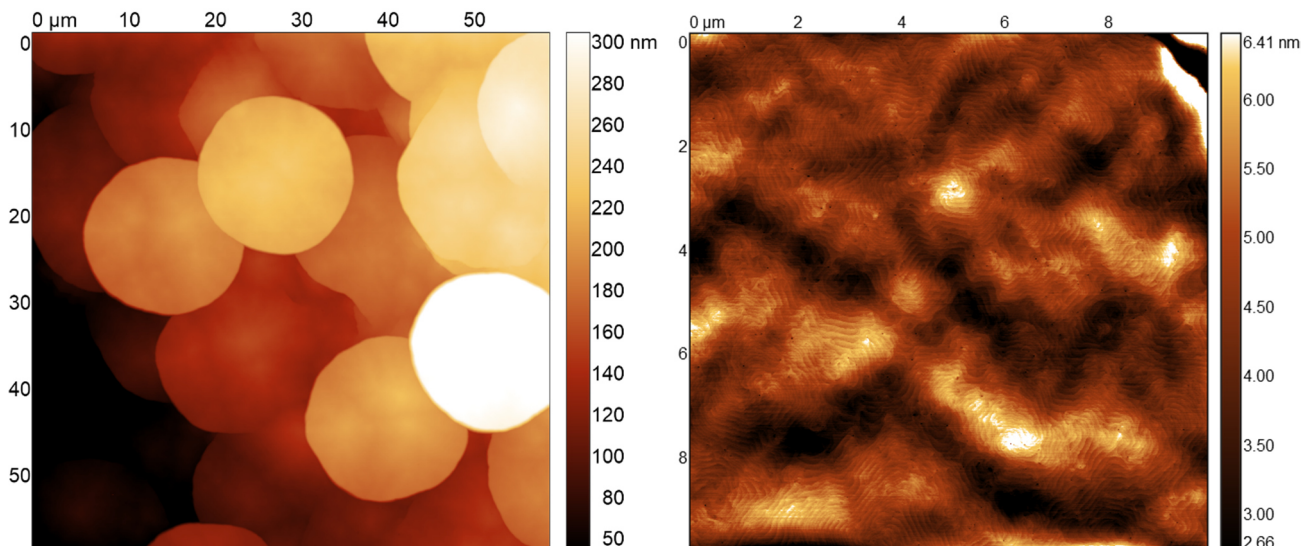


Figure 1 AFM images of surface of sample number 8. While the difference in height in the circular mesas is very large, up to 250 nm. The flatness of a single mesa is very good.

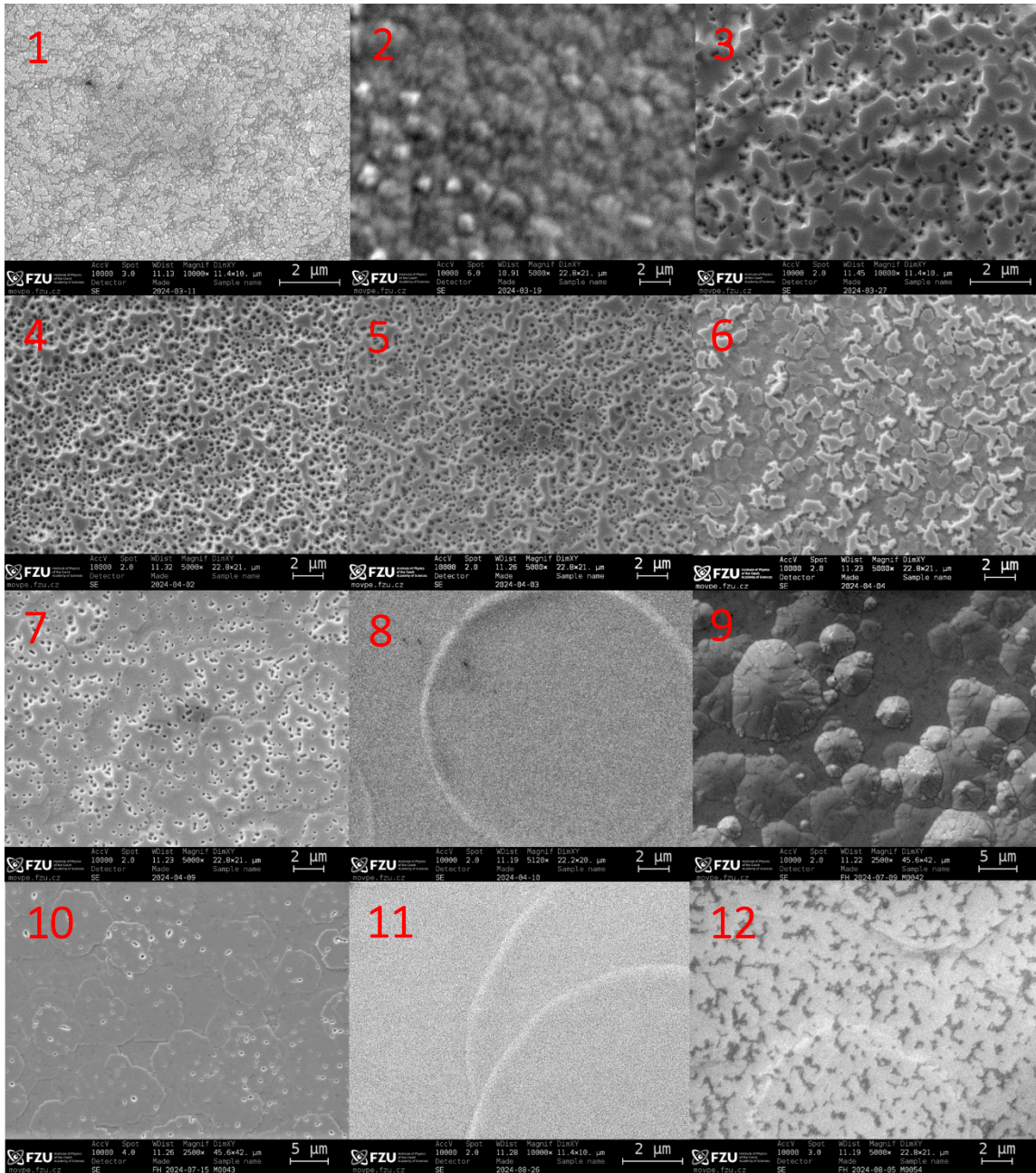


Figure 2 SEM image of first grown samples of AlGaIn on GaN nucleation layer. It is obvious that having AlGaIn coalesce into a flat surface with high crystalline quality is harder task than with GaN due to different adatom diffusion length of gallium and aluminium atom. This leads to slower coalescence and phase separation.

To assess the threading dislocation density XRD measurements were provided by Rotan laboratory complete with analysis and TDD calculations. Their results can be seen in graph (Figure 3) and table (Table 2). We could not have done the measurements on all samples prepared, but those will be done in the future. The slight decline in screw dislocations is promising for our future experiments.

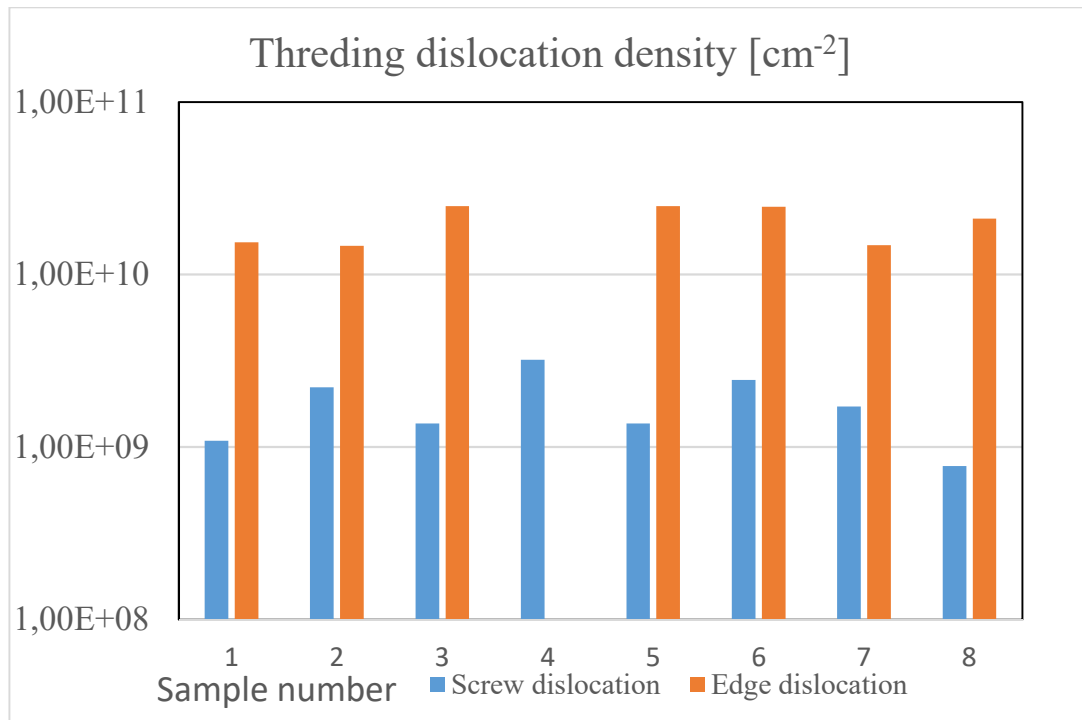


Figure 3 The graph of threading dislocation densities of measured sample in Rotan laboratory, the edge dislocations in sample number four could not be estimated due to asymmetric diffractions.

Table 2 Complimentary table for TDD measurements

1	2	3	4	5	6	7	M00
1,08E+09	2,21E+09	1,37E+09	3,19E+09	1,37E+09	2,45E+09	1,72E+09	7,74E+08
1,54E+10	1,46E+10	2,49E+10		2,49E+10	2,47E+10	1,48E+10	2,1E+10

Conclusions

We have made several samples of AlGa_N layers grown on sapphire substrates. We managed to achieve some interesting preliminary results. We found a recipe for an AlGa_N on sapphire substrate with the help of Ga_N nucleation and short coalescence without having any cracks in the surface layer. Also, we have found a way to make the AlGa_N smoother, as studied in SEM, except for the flat circular mesas. This surface structuring was further studied via AFM to get better assessment of the circular mesas. This problem will be tackled in our future experiments.

In regard to threading dislocation density there is still a lot of room for improvement, but given the fact that these are our first experiments, the results were better than expected. The threading dislocation density of measured samples via XRD was around 10¹⁰ of edge dislocations and 10⁹ screw dislocations, which is a good result. The eventual goal is getting 10⁸ of all dislocations which should be enough to reach sufficient external quantum efficiency of light emitting structures grown on top of the AlGa_N buffer layers.

References

- [1] NobelPrize.org, “The Nobel Prize in Physics 2014,” Mar. 30, 2024. [Online]. Available: <https://www.nobelprize.org/prizes/physics/2014/summary>
- [2] *Epitaxial growth of III-nitride compounds*. New York, NY: Springer Berlin Heidelberg, 2018.
- [3] Z. C. Feng, *III-nitride: semiconductor materials*. London: Imperial College press, 2006.
- [4] H. Morkoç, *Nitride semiconductor devices: fundamentals and applications*. Weinheim: Wiley-VCH, 2013.
- [5] S. Einfeldt *et al.*, “Strain in cracked AlGa_N layers,” *Journal of Applied Physics*, vol. 92, no. 1, pp. 118–123, Jul. 2002, doi: 10.1063/1.1481969.
- [6] J. A. Floro, D. M. Follstaedt, P. Provencio, S. J. Hearne, and S. R. Lee, “Misfit dislocation formation in the AlGa_N/Ga_N heterointerface,” *Journal of Applied Physics*, vol. 96, no. 12, pp. 7087–7094, Dec. 2004, doi: 10.1063/1.1812361.
- [7] Y. Ando *et al.*, “Non-planar growth of high Al-mole-fraction AlGa_N on patterned Ga_N platforms for mitigating strain-induced cracks beyond the critical layer thickness,” *Journal of Crystal Growth*, vol. 607, p. 127100, Apr. 2023, doi: 10.1016/j.jcrysgro.2023.127100.
- [8] C. F. Shih, N. C. Chen, S. Y. Lin, and K. S. Liu, “AlGa_N films grown on (0001) sapphire by a two-step method,” *Applied Physics Letters*, vol. 86, no. 21, p. 211103, May 2005, doi: 10.1063/1.1931058.

The authors acknowledge the support from Ministry of Education, Youth and Sport (MEYS) through OPJAK “Sendiso” project No. CZ.02.01.01/00/22_008/0004596.

Optimisation of deposition parameters of Ionised Jet Deposition (IJD) created Titanium nitride thin films

Bc. Martin Kolář, Ing. Jakub Skočdopole Ph.D.

Department of Solid State Engineering, Faculty of Nuclear Sciences and Physical Engineering, Czech Technical University in Prague

Abstract

Titanium nitride is often used as a protective coating due to its hardness. This material is mostly deposited by pulsed laser deposition or magnetron sputtering. Ionized jet deposition has a potential to improve and diversify ways of making titanium nitride thin films. We optimised the nitrogen pressure in the IJD chamber to suppress concentration of titanium oxide in films. We manufactured a set of films using different deposition pressures. Based on the XRD data, higher gas pressure is preferable. In contrast, lower gas pressure contributes to higher film growth, based on AFM data.

Keywords: IJD, TiN, thin films

Introduction

Titanium nitride is a material with wide range of applications. Thanks to its toughness, TiN is used as a protective layer for multitude of tools from drills to medical devices[1]. In electronics, TiN is used as diffusion barrier[2] or in newly emerging field of plasmonics[3].

Ionised Jet Deposition as a new method of thin film deposition has potential to create TiN films with better characteristic compared to older techniques. Thanks to high ionisation[4] of deposition gas it could be also possible to use titanium target instead of TiN target. IJD is also cheaper than other methods and could be easily scalable, so it is a perfect candidate for industrial application[5].

The aim of this research is to investigate deposition using titanium target, deposit series of thin films with different deposition pressures and analyse it by qualitative XRD analysis and AFM analysis to optimise deposition.

Materials and Methods

Initially AISI304 steel sheets were washed with water and soap solution, isopropyl alcohol with acetone, and pure acetone in ultrasonic bath respectively.

Thin titanium nitride layers on AISI304 steel sheets were deposited using IJD Jet-Dep100 system in Applied photonics and quantum technologies laboratory of Department of Solid State Engineering Faculty of Nuclear Sciences and Physical Engineering, Czech Technical University in Prague. Ultra-pure (99.99%) titanium target was used.

4 samples were deposited on room temperature for 30 minutes with 5 minutes conditioning of the target and IJD settings being: voltage 17 V, frequency 50 Hz, IJD-target distance 3 mm, IJD-substrate distance 110 mm. Nitrogen pressure varied between $1.9 \cdot 10^{-5}$ - $4.0 \cdot 10^{-5}$ mbar, see table 1.

Table 1: Gas pressure in IJD vacuum chamber

sample	TiN-1	TiN-2	TiN-3	TiN-4
Pressure before deposition [10^{-5} mbar]	4.2	6.0	3.5	3.4
Deposition gas pressure [10^{-4} mbar]	1.9	2.4	3.7	4.0

Thin film thickness was determined by measuring substrate-thin layer transition with Atomic Force Microscopy (AFM) using Akyama probe at laboratories of Applied photonics and quantum technologies. Phase composition was analysed by qualitative XRD analysis and by annealing of the samples. XRD patterns were obtained using grazing incidence geometry.

Results and Discussion

AFM

By analysing the substrate-thin layer transition from AFM using Gwyddion software the film thickness was determined, see table 2. There is a clear dependency of deposition growth rate on gas pressure, see fig. 1. By lowering gas pressure the deposition growth rate increases.

Table 2: Thin layer thickness

sample	TiN-1	TiN-2	TiN-3	TiN-4
Deposition gas pressure [10^{-4} mbar]	1.9	2.4	3.7	4.0
Thickness [nm]	250	210	200	190

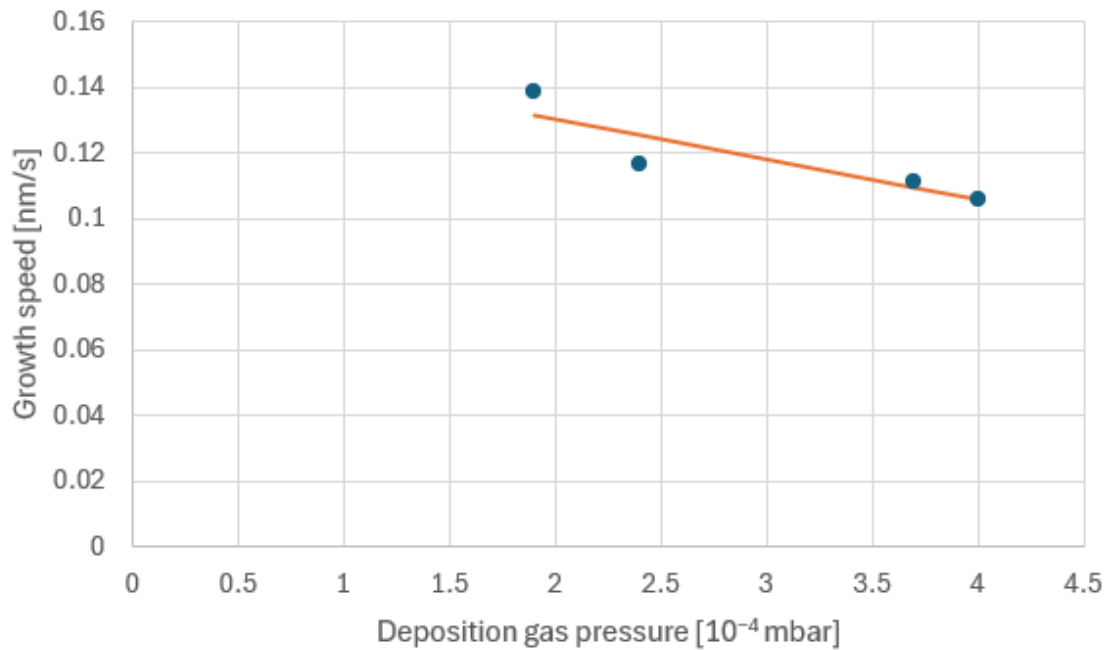


Figure 1: Dependency of layer growth rate on deposition gas pressure

XRD and Annealing

Qualitative phase analysis of the diffraction record of the TiN-1 sample, see figure 6 revealed that the most intense peaks belong to the steel substrate. Peaks were also found that may belong to both TiN and TiO, as both crystallise in the same lattice with very similar interplane distances [6][7]. The probable occurrence of hexagonal titanium in the sample was also revealed.

On the diffraction records of samples TiN-2, TiN-3 and TiN-4, see figures 3,4 and 5 respectively peaks from the steel substrate and peaks belonging to TiN or TiO were found.

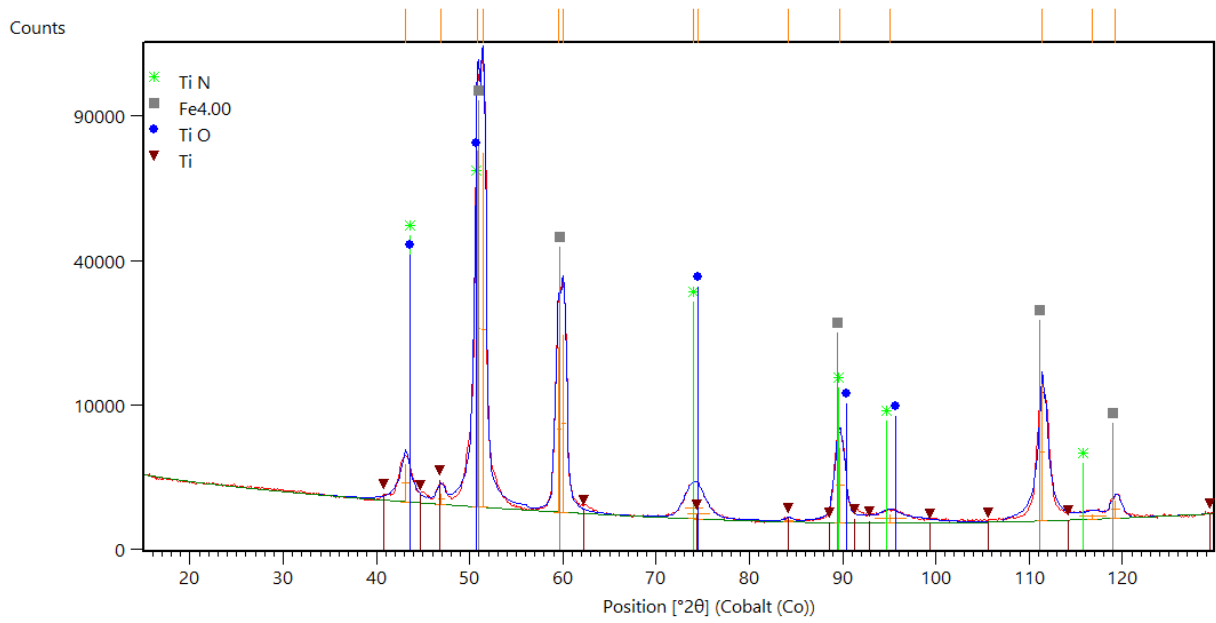


Figure 2: Diffraction record of sample TiN-1 measured under 3° angle for 9 h

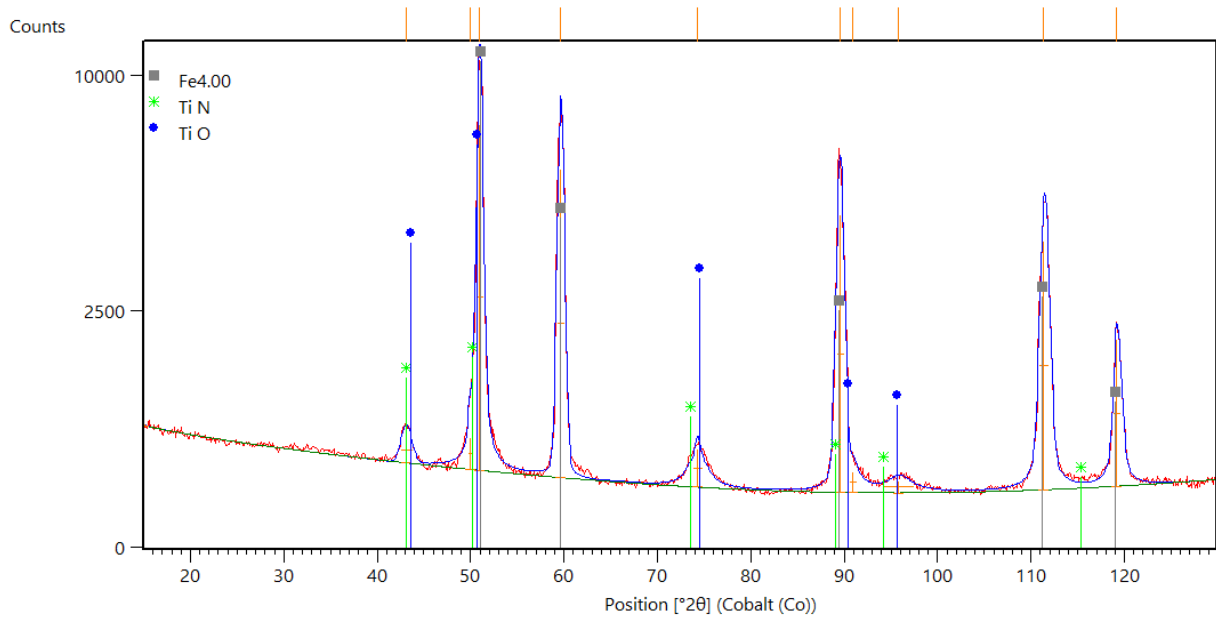


Figure 3: Diffraction record of sample TiN-2 measured under 3° angle for 5.75 h

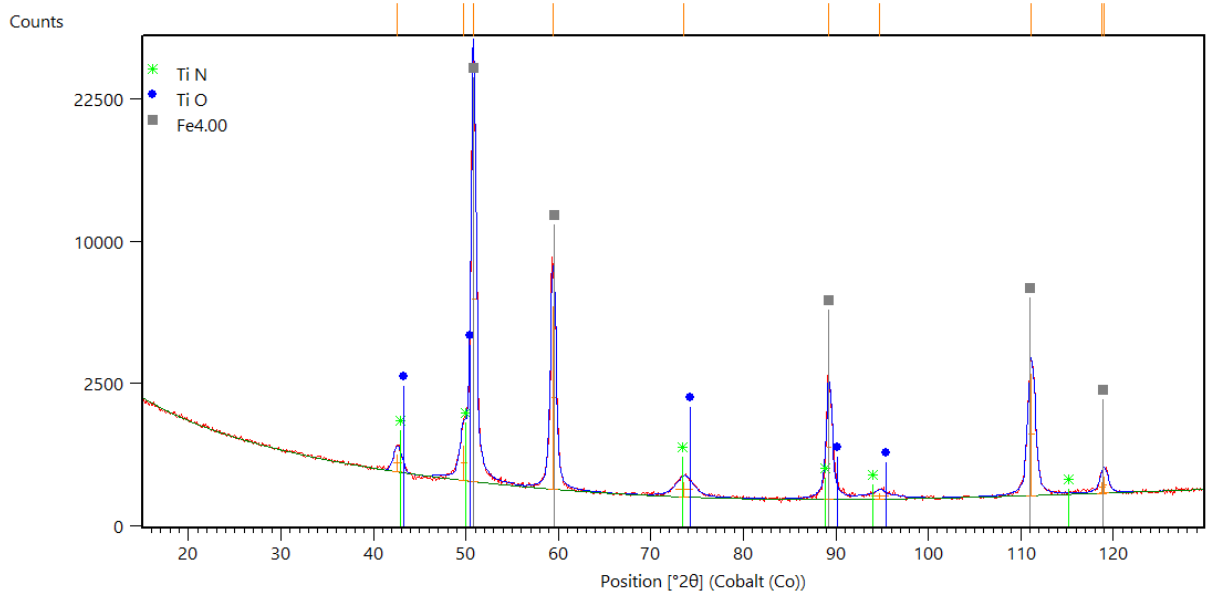


Figure 4: Diffraction record of sample TiN-3 measured under 1° angle for 3 h

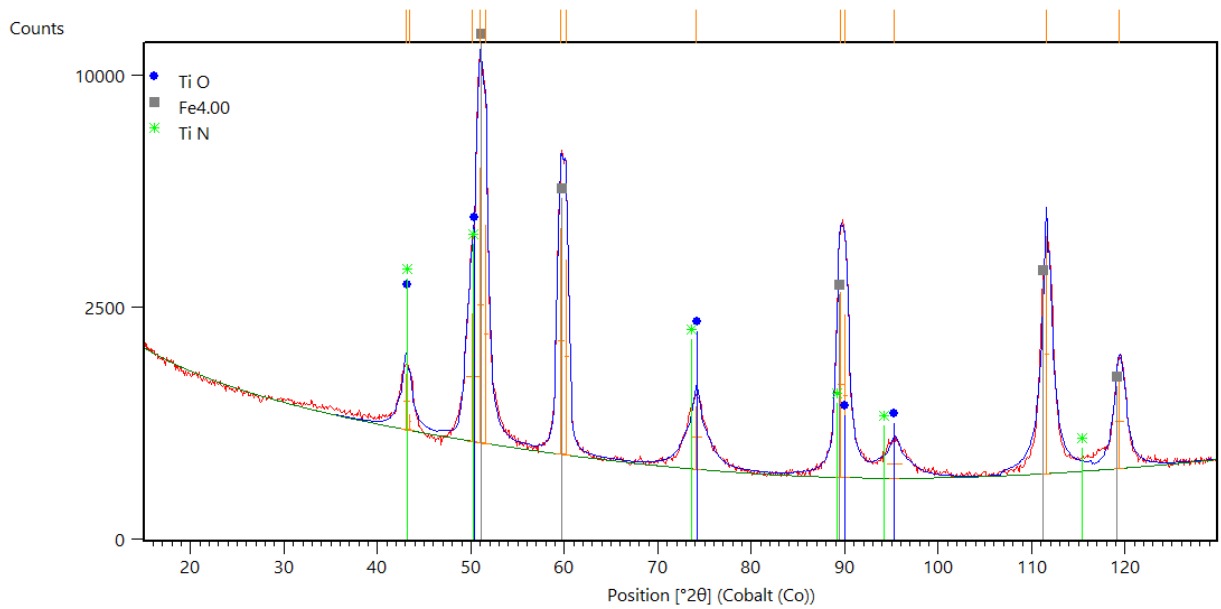


Figure 5: Diffraction record of sample TiN-4 measured under 3° angle for 3 h

After annealing the TiN-1 sample, there was a significant change in the color of the layer, see figure 6 and 7. On the diffraction record of the annealed sample, see image 11, steel from the substrate, TiN, TiO, hexagonal titanium and, newly TiO₂ were found. Other samples also changed colour after annealing, see pictures 8-10.

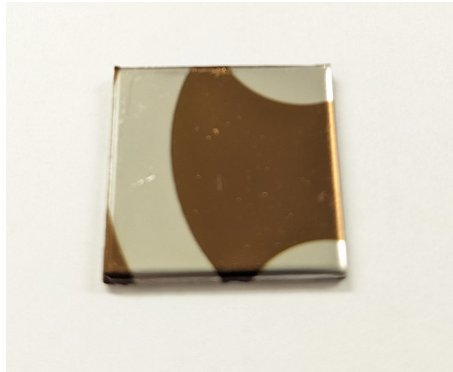


Figure 6: Not annealed TiN-1 thin film

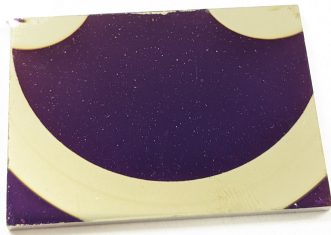


Figure 7: Annealed sample TiN-1



Figure 8: Annealed sample TiN-2

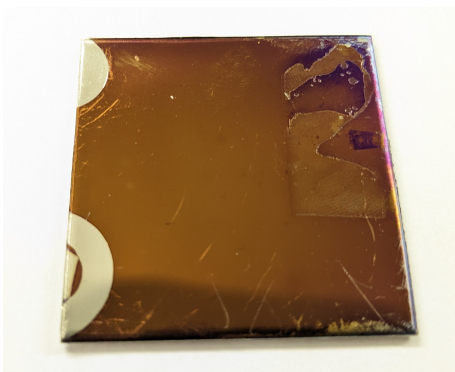


Figure 9: Annealed sample TiN-3

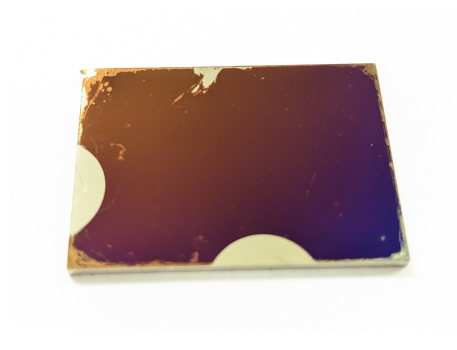


Figure 10: Annealed sample TiN-4

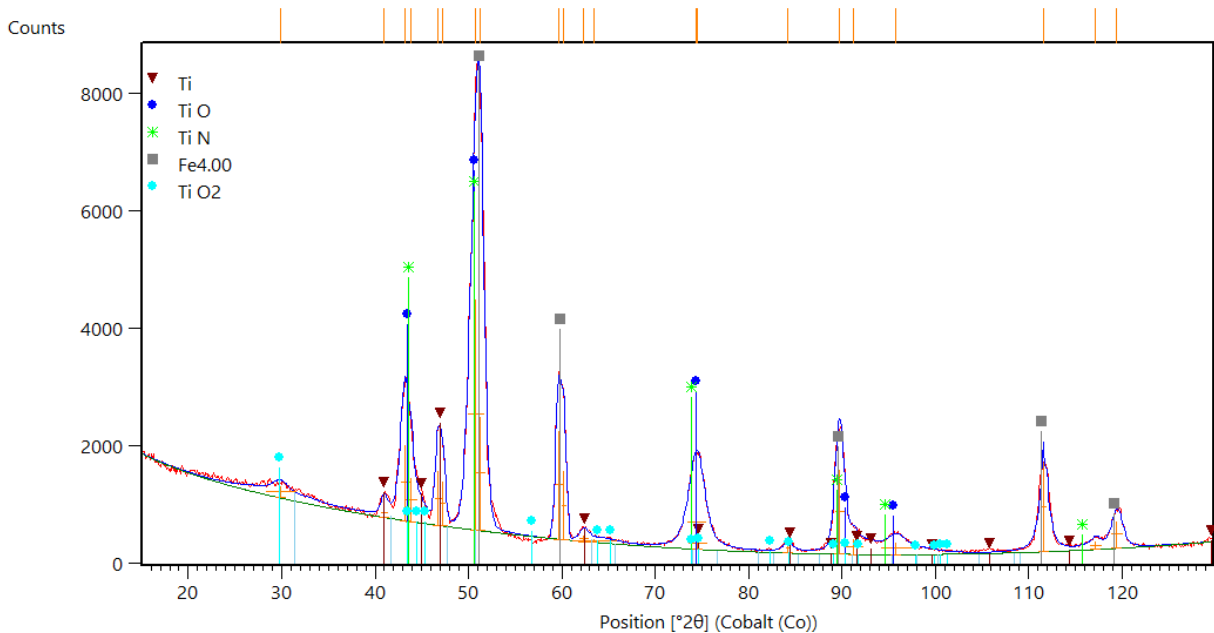


Figure 11: Diffraction record of annealed sample TiN-1 measured under 1° angle for 3.75 h

Hexagonal titan was only found in sample TiN-1 and after annealing TiO_2 peaks showed up. Also the colour of samples TiN-1 and TiN-2 changed more than of samples TiN-3 and TiN-4 probably because of lower concentration of TiN in samples TiN-3 and TiN-4 as TiN oxidises slower than titanium. Higher nitrogen pressure during deposition of samples TiN-3 and TiN-4 probably led to higher nitridation of samples.

Conclusions

Totally 4 samples were prepared. Thin film thickness analysis by AFM revealed indirect dependency of layer growth rate on deposition gas pressure. Qualitative XRD analysis together with annealing of the samples revealed that the nitridation of the thin films S directly proportional to the deposition gas pressure.

Problem with similar diffraction peaks of TiN and TiO need to be addressed in the next research. Use of silicon or glass as substrate would be preferred as it would allow use of more methods for analysis.

Reference

- [1] J.M. Lackner et al. "Structural, mechanical and tribological investigations of pulsed laser deposited titanium nitride coatings". In: *Thin Solid Films* 453-454 (2004). Proceedings of Symposium H on Photonic Processing of Surfaces, Thin Films and Devices, of the E-MRS 2003 Spring Conference, pp. 195–202. ISSN: 0040-6090. DOI: <https://doi.org/10.1016/j.tsf.2003.11.106>.

- [2] Violeta Merie et al. “Research on titanium nitride thin films deposited by reactive magnetron sputtering for MEMS applications”. In: *Applied Surface Science* 358 (2015), pp. 525–532. ISSN: 0169-4332. DOI: <https://doi.org/10.1016/j.apsusc.2015.07.063>.
- [3] Luca Mascaretti. “Plasmonic titanium nitride nanomaterials prepared by physical vapor deposition methods”. In: *Nanotechnology* 34 (2023). ISSN: 0169-4332. DOI: 10.1088/1361-6528/acfc4f.
- [4] J. Skočdopole. “Studium naprašování velmi tvrdých tenkých vrstev metodou IJD na podložky z legovaných oceli s přihlédnutím k aplikacím ve zdravotnictví”. MA thesis. Faculty of Nuclear Sciences and Physical Engineering CTU, 2017.
- [5] Noivion. *IONIZED JET DEPOSITION*. [Online; accessed 19.6.2024]. 2013. URL: <https://noivion.com/technology/>.
- [6] Materials Project. *TiN (mp-492) from database version v2023.11.1*. [Online; accessed 30.7.2024]. URL: <https://next-gen.materialsproject.org/materials/mp-492#more>.
- [7] Materials Project. *TiO (mp-2664) from database version v2023.11.1*. [Online; accessed 30.7.2024]. URL: <https://next-gen.materialsproject.org/materials/mp-2664>.

Acknowledgement

This work was supported by the Grant Agency of the Czech Technical University in Prague, grant No. SGS22/183/OHK4/3T/14.

AA bilayer coupler

Petr Červenka¹

¹Department of Physics, Faculty of Nuclear Sciences and Physical Engineering, Czech Technical University in Prague
cervep12@cvut.cz

Abstract

Two non-interacting graphene sheets are deformed in a localized region where they form *AA* bilayer graphene. This theoretical model is called the *AA* bilayer coupler. We show that the Hamiltonian of this system can be elegantly block-diagonalized. On the coupler, the scattering properties of Dirac fermions in two dimensions are analyzed through a partial wave decomposition. The differential and partial cross sections reveal some interesting phenomena, such as pouring particles from one layer to the other, filtering Dirac fermions with a given value of angular momentum, or the formation of quasi-bound states.

Keywords: *AA* bilayer graphene; Dirac equation; scattering, solvable models.

Introduction

Rapid scientific progress in the field of 2D materials demands a theoretical description of their physical properties. Graphene is a two-dimensional material [1] which further belongs to the family of Dirac materials [2]. These materials have at least one common property. A great part of the underlying physics behind these materials is governed by the Dirac equation. Low-energy quasiparticles in graphene behave like massless relativistic fermions as they are described by the 2D Dirac equation. Graphene is thus a perfect playground for simulating relativistic quantum physics on the table-top experiments.

There exist multilayered derivatives of graphene. Especially, bilayer graphene enjoys a great deal of research interest because of its many interesting properties. Famous ones are superconducting twisted bilayer [3], anomalous quantum Hall effect [4] or energy gap which can be tuned by an external electric field [5]. In addition to pseudospin and valley polarization coming from graphene, the bilayer brings the layer degree of freedom to the game.

For better understanding of physical phenomena in graphene or bilayer graphene, it is necessary to deal with the 2D Dirac equation. Solvable models in this area usually rely on translational or rotational symmetry so that the evolution equation can be reduced to one dimension [6].

Electron transport sometimes requires transfer from one channel to another. Devices that suit this task are called couplers. We show that two non-interacting parallel graphene sheets can work as a coupler if they turn into *AA* bilayer in a restricted area. We denote this device as *AA* bilayer coupler. It is worth mentioning that the experimental implementation of a related *AB* bilayer coupler was already done in [7].

1 Model of AA bilayer coupler

The Hamiltonian that describes the physical model of a coupler is

$$H = \begin{pmatrix} H_0 & t\theta(R-r) \\ t\theta(R-r) & H_0 \end{pmatrix}, \quad (1)$$

$$H_0 = -i \left[\sigma_r \partial_r + \frac{1}{r} \sigma_\varphi \partial_\varphi \right], \quad \sigma_r = \begin{pmatrix} 0 & e^{-i\varphi} \\ e^{i\varphi} & 0 \end{pmatrix}, \quad \sigma_\varphi = i \begin{pmatrix} 0 & -e^{-i\varphi} \\ e^{i\varphi} & 0 \end{pmatrix}.$$

Where we have introduced a constant hopping parameter $t \in \mathbb{R}$ and a radius $R > 0$ of the AA bilayer graphene region. The ordering of the wavefunction is $\Psi = (\psi_{A1}, \psi_{B1}, \psi_{A2}, \psi_{B2})$ (sublattice A, B ; layer 1, 2). We would like to analyze the scattering of Dirac particles on a coupler. The first step is to solve the eigenvalue equation of H . A great simplification of this task is achieved by the following unitary transformation $U = e^{i\frac{\pi}{4}\sigma_2} \otimes \mathbb{I}$

$$UHU^\dagger = \left(\begin{array}{c|c} H_0 + t\theta(R-r) & 0 \\ \hline 0 & H_0 - t\theta(R-r) \end{array} \right). \quad (2)$$

The eigenvalue equation $UHU^\dagger U\Psi = EU\Psi, U\Psi(r, \varphi) = (\psi(r, \varphi), \chi(r, \varphi))^T$ takes the form

$$\begin{pmatrix} H_0 + t\theta(R-r) & 0 \\ 0 & H_0 - t\theta(R-r) \end{pmatrix} \begin{pmatrix} \psi \\ \chi \end{pmatrix} = E \begin{pmatrix} \psi \\ \chi \end{pmatrix} \iff \begin{cases} H_0\psi = [E - t\theta(R-r)]\psi \\ H_0\chi = [E + t\theta(R-r)]\chi. \end{cases} \quad (3)$$

On the right-hand side, there are two 2D Dirac equations where the energy is shifted by a constant t at $r < R$. We focus on the equation for $\psi(r, \varphi)$ and make the ansatz $\psi(r, \varphi) = e^{im\varphi}(\psi_A(r), ie^{i\varphi}\psi_B(r))^1$. By the action of H_0 given by (1) on this ansatz, we separate the variables r and φ and get the coupled equations in variable r only

$$\begin{aligned} \left(\partial_r + \frac{m+1}{r} \right) \psi_B(r) &= [E - t\theta(R-r)] \psi_A(r) \\ \left(-\partial_r + \frac{m}{r} \right) \psi_A(r) &= [E - t\theta(R-r)] \psi_B(r). \end{aligned} \quad (4)$$

Decoupling the equations provides us the Bessel equation for $\psi_A(r)$ component

$$\psi_A'' + \frac{1}{r}\psi_A' + \left[(E - t\theta(R-r))^2 - \frac{m^2}{r^2} \right] \psi_A = 0. \quad (5)$$

The solution is known in Bessel (J_m, Y_m) or Hankel ($H_m^{(1)}, H_m^{(2)}$) functions. Before that, it is necessary to distinguish the domains $r > R$ and $r < R$ due to the discontinuity of the step

¹ $m \in \mathbb{Z}$ is the quantum number related to the total angular momentum $J_3\psi = (-i\partial_\varphi + 1/2\sigma_3)\psi = (m + 1/2)\psi$.

function θ . In summary, the wavefunction is sum over all m 's ($C_1^{(m)}, C_2^{(m)}, S_1^{(m)}, S_2^{(m)} \in \mathbb{C}$)

$$\psi(r, \varphi) = \begin{cases} \sum_{m=-\infty}^{+\infty} e^{im\varphi} \left[C_1^{(m)} \begin{pmatrix} J_m(k_- r) \\ i\xi_- e^{i\varphi} J_{m+1}(k_- r) \end{pmatrix} + C_2^{(m)} \begin{pmatrix} Y_m(k_- r) \\ i\xi_- e^{i\varphi} Y_{m+1}(k_- r) \end{pmatrix} \right], & r < R \\ \sum_{m=-\infty}^{+\infty} e^{im\varphi} \left[S_1^{(m)} \begin{pmatrix} H_m^{(1)}(kr) \\ i\xi e^{i\varphi} H_{m+1}^{(1)}(kr) \end{pmatrix} + S_2^{(m)} \begin{pmatrix} H_m^{(2)}(kr) \\ i\xi e^{i\varphi} H_{m+1}^{(2)}(kr) \end{pmatrix} \right], & r \geq R, \end{cases} \quad (6)$$

where we have defined $k = |E|$, $k_{\pm} = |E \pm t|$, $\xi = \text{sgn}(E)$, $\xi_{\pm} = \text{sgn}(E \pm t)$. The component $\psi_B(r)$ is calculated from the second line of (4) where we have used the recurrence $(-\partial_r + m/r)J_m(kr) = kJ_{m+1}(kr)$. We proceed analogously for χ . The wavefunction Ψ is recovered from $\Psi = U^\dagger(\psi, \chi)$. The regularity of Ψ in $r = 0$ forces us to discard the Bessel function Y_m due to its divergence $Y_m(0) = \pm\infty$. The explicit eigenfunctions of the coupler Hamiltonian, which will be further used in the text, can be written as ($\alpha = \pm 1$)

$$\Psi = \begin{cases} \sum_{m=-\infty}^{+\infty} i^m e^{im\varphi} \left[C_1^{(m)} \begin{pmatrix} J_m(k_- r) \\ i\xi_- e^{i\varphi} J_{m+1}(k_- r) \\ J_m(k_- r) \\ i\xi_- e^{i\varphi} J_{m+1}(k_- r) \end{pmatrix} + C_2^{(m)} \begin{pmatrix} -J_m(k_+ r) \\ -i\xi_+ e^{i\varphi} J_{m+1}(k_+ r) \\ J_m(k_+ r) \\ i\xi_+ e^{i\varphi} J_{m+1}(k_+ r) \end{pmatrix} \right], & r < R \\ \sum_{m=-\infty}^{+\infty} i^m e^{im\varphi} \left[\begin{pmatrix} J_m(kr) \\ i\xi e^{i\varphi} J_{m+1}(kr) \\ 0 \\ 0 \end{pmatrix} + S_1^{(m)} \begin{pmatrix} H_m^{(\frac{3-\alpha}{2})}(kr) \\ i\xi e^{i\varphi} H_{m+1}^{(\frac{3-\alpha}{2})}(kr) \\ 0 \\ 0 \end{pmatrix} + S_2^{(m)} \begin{pmatrix} 0 \\ 0 \\ H_m^{(\frac{3-\alpha}{2})}(kr) \\ i\xi e^{i\varphi} H_{m+1}^{(\frac{3-\alpha}{2})}(kr) \end{pmatrix} \right], & r \geq R. \end{cases} \quad (7)$$

The scattering setup consists of an incoming plane wave Ψ_{in} which hits the AA bilayer region. After that, it is scattered in the form of a circular wave Ψ_{sc} . For the investigation of the coupling properties, we assume an incoming wave localized on the layer 1. The scattering states have to satisfy the asymptotical behavior for large r ($\alpha = \pm 1$)

$$\Psi_{in} + \Psi_{sc} \sim \frac{1}{\sqrt{2}} \begin{pmatrix} 1 \\ 1 \\ 0 \\ 0 \end{pmatrix} e^{i\xi kx} + \frac{1}{\sqrt{2}} \begin{pmatrix} f_E^{(A1)}(\varphi) \\ f_E^{(B1)}(\varphi) \\ f_E^{(A2)}(\varphi) \\ f_E^{(B2)}(\varphi) \end{pmatrix} \frac{e^{i\alpha kr}}{\sqrt{r}}. \quad (8)$$

We have already chosen the part $r \geq R$ of the wavefunction Ψ given by (7) such that it satisfies the asymptotics (8). This can be proven if we realize $e^{ikx} = \sum_m i^m e^{im\varphi} J_m(kr)$ and the asymptotical behavior of Hankel functions $H_m^{(\frac{3-\alpha}{2})}(kr) \stackrel{r \gg 1}{\approx} \sqrt{\frac{2}{rk\pi}} e^{-i\alpha(m\pi/2 + \pi/4)} e^{i\alpha kr}$ [8]. Whether we take $\alpha = 1$ or $\alpha = -1$ depends on the sign of the radial probability current $\Psi_{sc}^\dagger \sigma_r \Psi_{sc}$. The scattered particles should propagate from the scattering region (not to) so the requirement $\Psi_{sc}^\dagger \sigma_r \Psi_{sc} > 0$ fully specifies α .

The scattering amplitudes $f_E^{(A1)}, \dots, f_E^{(B2)}$ in (8) encode the angle dependence of the scattered wave, i.e. there could exist directions φ in which scattering takes place more prominently. However, the scattering amplitudes have yet unknown constants $C_{1,2}^{(m)}, S_{1,2}^{(m)}$. Those constants are uniquely determined by the requirement of continuity of Ψ in $r = R$, that is $\forall \varphi \in [0, 2\pi) : \lim_{r \rightarrow R^+} \Psi(r, \varphi) = \lim_{r \rightarrow R^-} \Psi(r, \varphi)$. The scattering amplitudes are

connected to experimentally measurable *differential cross section* $d\sigma^{(1,2)}/d\varphi$ for layer 1 and 2

$$\frac{d\sigma^{(1)}}{d\varphi} = \text{Re} \left(f_E^{(A1)} \overline{f_E^{(B1)}} e^{i\varphi} \right), \quad \frac{d\sigma^{(2)}}{d\varphi} = \text{Re} \left(f_E^{(A2)} \overline{f_E^{(B2)}} e^{i\varphi} \right). \quad (9)$$

The differential cross section is proportional to the probability that the Dirac fermions are scattered at the angle φ . Integrating over all angles gives us total cross section

$$\sigma^{(1,2)}(E) = \int_0^{2\pi} \frac{d\sigma^{(1,2)}}{d\varphi} d\varphi = \sum_{m=-\infty}^{+\infty} \sigma_m^{(1,2)}(E). \quad (10)$$

The elements $\sigma_m^{(1,2)}$ are called *partial cross sections*. They describe the scattering of particles with fixed angular momentum quantum number m . It corresponds to the scattering situation when we take the incoming wave as $e^{im\varphi} (J_m(kr), i\xi e^{i\varphi} J_{m+1}(kr), 0, 0)^T$ instead of $e^{i\xi kx} (1, 1, 0, 0)^T$.

2 Results and Discussion

The partial cross sections are shown in Fig. 1. As $\sigma_m^{(2)} \neq 0$, the incoming Dirac fermions from layer 1 can be transferred to layer 2. The values of $\sigma_m^{(2)}$ and $\sigma_m^{(1)}$ do not differ much,

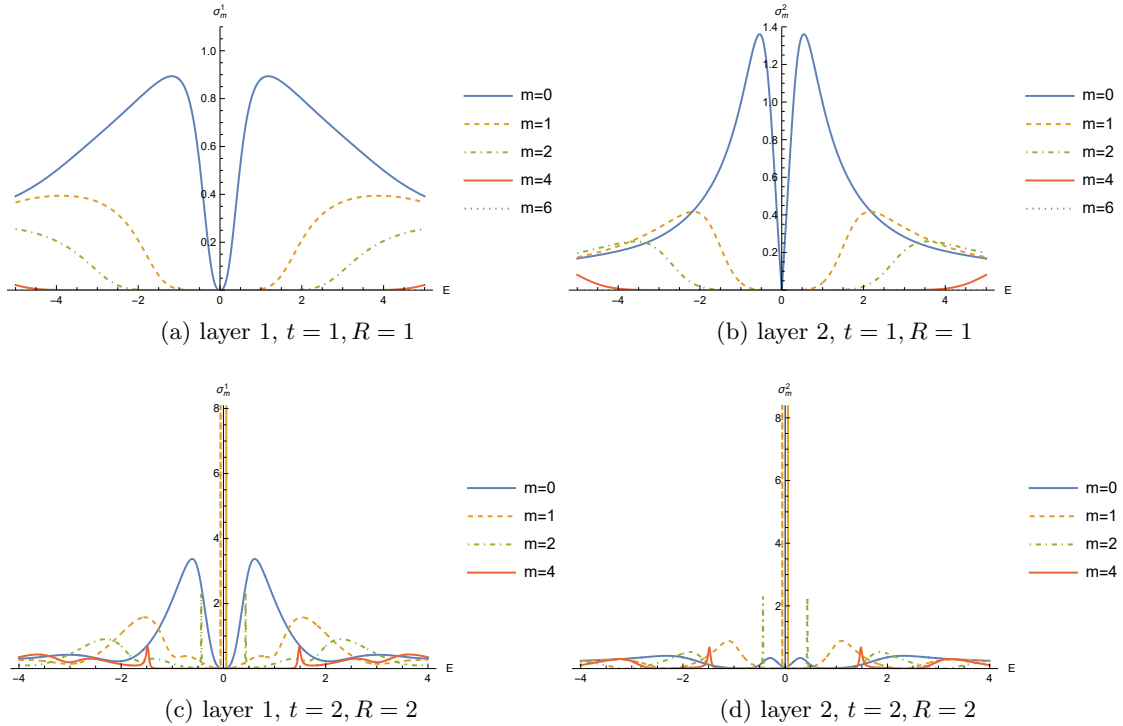


Figure 1: (*Color online*) The partial cross sections $\sigma_m^{(1,2)}(E)$ given by (10) plotted as a function of the incoming wave energy E . The radius R and hopping parameter t are below each figure.

so the transfer should not be highly inefficient. Both $\sigma_m^{(1)}$ and $\sigma_m^{(2)}$ exhibit peaks that point to the resonances of states with given m (quasi-bound states) inside the AA bilayer region. States with the energy of the peaks are trapped for a finite time in the AA bilayer region. Narrower peaks mean longer trapping time. Deeper analysis of the trapping time can be found in [9].

The peaks become narrower if we increase R (and thus the area) of AA bilayer or if we increase the strength of the coupling t . These increases cause a higher possibility of particle interaction with the scattering region. We can further observe that there exist energies for which, except for one specific m , all partial cross sections vanish. For example, it is state $m = 0$ and $E \approx 0.5$ in Fig. 1b or $m = 1$ and $E \approx 0.02$ in Fig. 1d. The scattering of states with a quantum number m on layer 2 does not take place if the corresponding $\sigma_m^{(2)}$ vanishes. Based on this observation, we can construct a filter that passes states with one selected m to layer 2.

From the differential cross sections in Fig. 2, it is evident that the scattering is strongly anisotropic. The absence of backscattering at the angle $\varphi = \pi$ can be useful because no

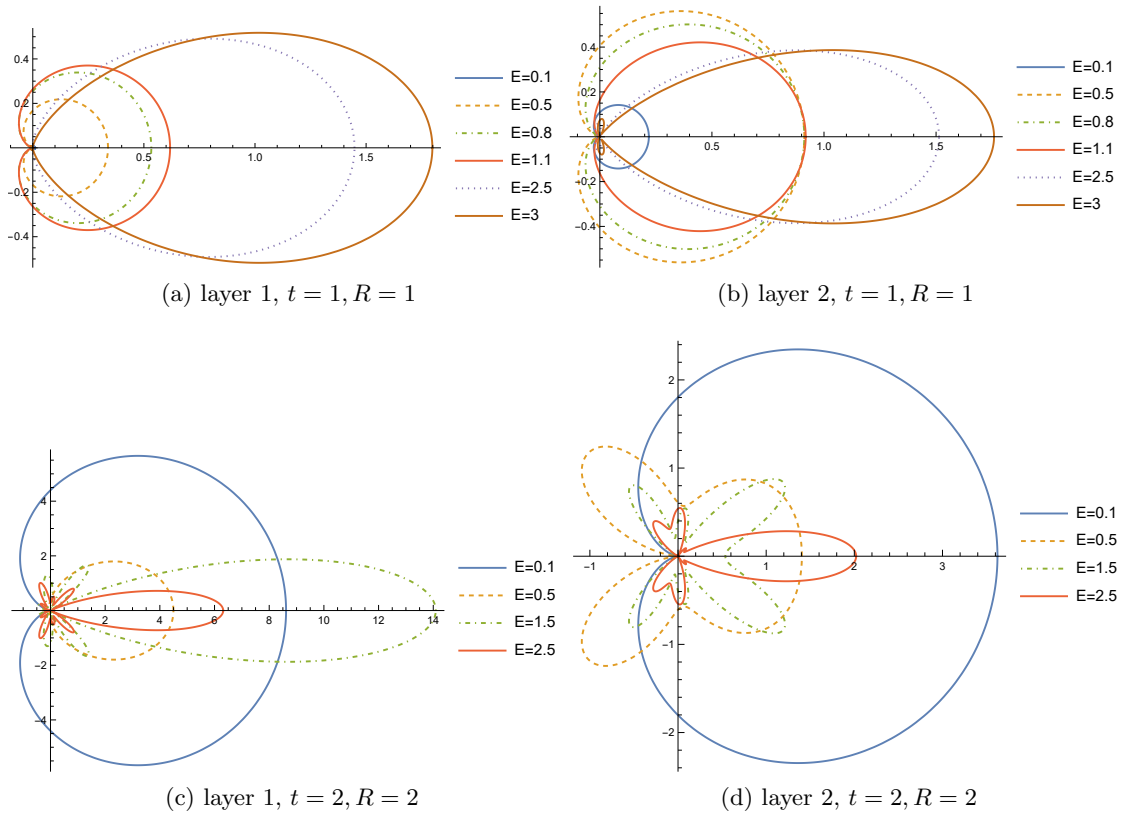


Figure 2: (*Color online*) The differential cross sections $d\sigma^{(1,2)}/d\varphi$ given by (9) plotted as polar graphs in variable φ .

particles return to the source that emits incoming Dirac fermions (in the form of plane waves). Let us summarize the most significant results obtained from the analysis of partial and differential cross sections:

1. The coupler can transfer incoming particles from layer 1 to layer 2.

2. There is no phenomenon in which the scattering on one layer somehow substantially outweighs the scattering on the other layer. If it did happen, it would be ineffective to transfer Dirac fermions between layers.
3. We are able to fully filter out the $m = 0$ state from an incoming plane wave on layer 2 (see Fig. 1b). Higher values of R and t allow us to separate states with higher m (state $m = 1$ in Fig. 1d).
4. Dirac fermions go mostly through the AA region in the direction $\varphi = 0$ (see Fig. 2). The absence of backscattering is also clearly visible there.
5. The peaks in the partial cross sections point to the formation of quasi-bound states in the coupling AA region.
6. The scattering pattern of low-energy fermions in layer 2 is robust to the change of R, t . This observation is based on the layer 2 blue line ($E = 0.1$) in Fig. 2 where the blue line retains the shape of the cardioid.

3 Conclusions

Our aim was to qualitatively analyze the scattering of Dirac particles on a solvable model called the AA bilayer coupler. The 2D scattering method is quite general and can also be used for AB or more exotic graphene bilayers. The 2D Dirac equation is not even limited to the physics of graphene but is valid for all 2D Dirac materials such as transition metal dichalcogenides². To the originally intended proof of particle transfer between layers, we have discovered additional possibilities for the use of the coupler. In the future, we would like to study these in more complex physical conditions, e.g. in the presence of electric or magnetic fields.

References

- [1] Mikhail I. Katsnelson. *The Physics of Graphene*. 2 edition. Cambridge University Press, 2020.
- [2] Wehling, T.O. and Black-Schaffer, A.M. and Balatsky, A.V. Dirac materials. *Advances in Physics* **63**(1): 1-76, 2014.
- [3] Yuan Cao, Valla Fatemi, Shiang Fang, Kenji Watanabe, Takashi Taniguchi, Efthimios Kaxiras, and Pablo Jarillo-Herrero. Unconventional superconductivity in magic-angle graphene superlattices. *Nature* **556**(7699): 43-50, 2018.
- [4] Edward McCann and Vladimir I. Fal'ko. Landau-Level Degeneracy and Quantum Hall Effect in a Graphite Bilayer. *Physical Review Letters* **96**(8): 086805, 2006.
- [5] Yuanbo Zhang, Tsung-Ta Tang, Caglar Girit, Zhao Hao, Michael C. Martin, Alex Zettl, Michael F. Crommie, Y. Ron Shen, and Feng Wang. Direct observation of a widely tunable bandgap in bilayer graphene. *Nature* **459**(7248): 820–823, 2009.
- [6] Charles A. Downing and Mikhail E. Portnoi. Zero-Energy Vortices in Dirac Materials. *physica status solidi (b)* **256**(9): 1800584, 2019.

²They consist of chalcogen (S, Se, Te) and transition metals (Ti, V, Mo, Pd, Pt...), e.g. MoS₂, WS₂, PtTe₂.

- [7] Yung-Chang Lin, Amane Motoyama, Pablo Solís-Fernández, Rika Matsumoto, Hiroki Ago, and Kazu Suenaga. Coupling and Decoupling of Bilayer Graphene Monitored by Electron Energy Loss Spectroscopy. *Nano Letters* **21**(24): 10386–10391, 2021.
- [8] Milton Abramowitz and Irene A. Stegun. *Handbook of Mathematical Functions with Formulas, Graphs, and Mathematical Tables*. Dover, New York, ninth Dover printing, tenth GPO printing edition, 1964.
- [9] Ş. Kuru, J. Negro, L.M. Nieto, and L. Sourrouille. Massive and massless twodimensional Dirac particles in electric quantum dots. *Physica E: Low-dimensional Systems and Nanostructures* 142:115312, 2022.

Acknowledgement

This work was supported by the Grant Agency of the Czech Technical University in Prague, grant No. SGS13/219/OHK4/3T/14, and Czech Science Foundation, grant No. 14-36566G.

The real structure of γ -Fe phase of rolled 1.4470 duplex steel after shot peening

M. Rušin, J. Čapek, K. Trojan, N. Ganev

Department of Solid State Engineering, Faculty of Nuclear Sciences and Physical Engineering,
Czech Technical University in Prague

Abstract

Duplex stainless steels exhibit better properties, such as corrosion resistance, compared to single-phase steels. They are widely used in many engineering areas. Shot peening is commonly used technique in surface machining. It is used to further improve the final properties, such as service life. It is essential to know how this process affects the so-called real structure, which to great extent determines the final properties of the steel. The impact of shot peening intensity on crystallite size, residual stresses and preferred orientation was studied. It was found that shot peening caused a reduction in crystallite size in subsurface layers. It also led to an increase in compressive residual stresses in near-surface regions. The influence on preferred orientation was not as strong, yet some crystallites were rotated and reoriented.

Key words: X-ray diffraction; Duplex steel; Shot peening; Real structure.

Introduction

Duplex stainless steels (DSS) are a family of grades which provides significantly greater strength than the austenitic grades, while exhibiting good ductility and toughness. They also exceed austenitic grades in corrosion resistance, which is primarily a function of their alloying elements such as chromium, molybdenum, tungsten, and nitrogen. Due to their mechanical, corrosion properties, and reduced cost, DSS are widely used in areas such as automotive, aviation industry, civil engineering, and food storage. Metallurgy of DSS changes with chemical composition and manufacturing processes. Two main phases are ferrite (α -Fe) and austenite (γ -Fe), mostly in a 1:1 ratio. [1]

Shot Peening (SP) is used to further improve the final mechanical properties of the materials. This technique involves bombarding the machined piece with small spherical media. As a result, the material's surface undergoes plastic deformation. This leads to generation of compressive residual stresses in the surface and subsurface regions of the peened material. Compressive stresses provide considerable increase in service life, since crack initiation, fatigue, and stress corrosion failures are reduced in a compressively stressed zone. Apart from residual stresses, SP also influences other parameters. Cold-working effect of SP causes increase in surface hardness due to work hardening, surface texturing or closing of porosity. [2]

The anisotropy of macroscopic properties of materials, such as DSS, is influenced by their real structure, which may change during the mechanical or thermal processing. Therefore, it is necessary to determine and describe the real structure and its depth profile after the rolling and SP. X-ray diffraction techniques were used to evaluate the impact of SP intensity on crystallite size, residual stresses, and preferred orientation (texture). The depth distributions of these parameters in γ -Fe phase are described.

Experiment

Three samples were produced from 1.4470 DSS plate of 3 mm thickness. At first, the plate was annealed at a temperature of 650 °C for 7 hours and cold rolled to half of the original thickness – 1,5 mm. Additional annealing was applied to reduce the residual stresses originating from the previous processing. Several samples were created by cutting the plate into smaller pieces. Three of them were chosen for this study. One, which was not shot peened for reference, was labelled N, and two peened with pressure 1.5 bar and 7 bar were denoted P1.5 and P7, respectively. Rolling (RD), transversal (TD), and normal (ND) directions created their coordination system. SP treatment was carried out using quenched steel shots with diameter 0,43 mm. Using air pressure 1,5 and 7 bar, the intensity of $9,00 \pm 0,01$ and $1,90 \pm 0,08$ mmA, respectively, was achieved. SP intensity was measured by the arc height of A type Almen strip. The SP direction was the same as the RD.

The XRD patterns were collected by *Empyrean PANalytical* diffractometer with manganese X-ray tube. In order to obtain the depth distributions of above-mentioned parameters, the samples were gradually electrochemically polished using *PROTO Electrolytic polisher 8818-V3* with A2 electrolyte. The diffraction lines were analysed using *PANalytical* software package containing *DataViewer* for basic peak parameters and *X'Pert Stress* for stress analysis. Crystallite size was calculated using the Scherrer formula analysed by $\{220\}$ diffraction line. The $\{311\}$ diffraction line was used to analyse the residual stress distribution using “ $\sin^2 \psi$ ” method assuming the bi-axial state of the residual stresses with respect to RD and TD axis. The MATLAB™ MTEX toolbox programme [3] was used to calculate orientation distribution function (ODF). The ODF calculated from the experimental pole figures obtained by analysis of $\{111\}$, $\{200\}$, and $\{220\}$ diffraction lines was used for texture analysis.

Results and discussion

The results of crystallite size analysis are shown in Fig. 1. For sample N, only the values from surface and first measured depth are shown. The size of crystallites at the surface was 20 nm and at the first measured depth 23 nm. With increasing depth, the values fluctuated around 24 nm. The difference between two first values are caused by grinding and rolling, which influences near-surface layer more than regions deeper in the material.

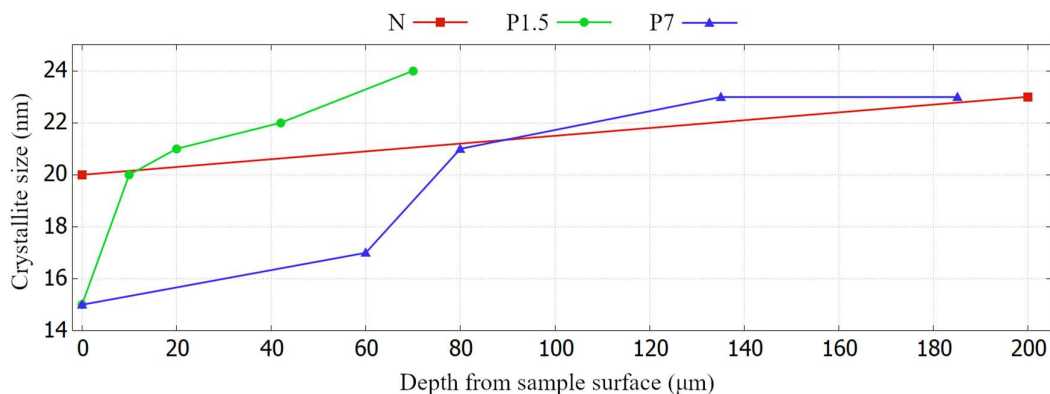


Figure 1. The depth distributions of the crystallite size analysed by using $\{220\}$ diffraction line.

After SP, the crystallites were reduced in their size. Its value was 15 nm at the surface, for both peened samples. With increasing distance from the sample surface, the crystallite size changed to values comparable to those for sample N. As can be seen, SP with higher intensity caused size reduction extending to deeper regions. For sample P1.5, crystallites were as big as those for sample N already from a depth of 10 μm . In deeper regions they were even bigger, which is caused by heterogenous microstructure of all samples before SP. For sample P7 the affected zone reaches up to 80 μm from sample surface.

Residual stresses in RD are shown in Fig. 2. The low tensile residual stresses were on the surface of sample N and could be neglected within the measurement error. As expected, SP led to an increase in compressive residual stresses (CRS) in near-surface regions. The largest values were directly at the surface, namely around 560 MPa for sample P1.5. As the depth increased, the values gradually decreased. At 40 μm from sample surface they transformed into tensile stresses with negligible values within the measurement error as in the case of sample N. Compared to P1.5, sample P7 had lower CRS at the surface with value around 400 MPa. However, at greater depths the residual stresses were more affected. The CRS reached their maximum values of about 700 MPa at a 60 μm depth. At the deepest measured region, the residual stresses decreased as for sample P1.5. More intense SP caused higher values of CRS deeper in the sample. On the other hand, the sample surface was more affected by SP with lower intensity. The reason is that the blasted balls did not have sufficient intensity to affect deeper areas of the material, but at the same time were capable of significantly deforming the surface and thus causing large residual stresses.

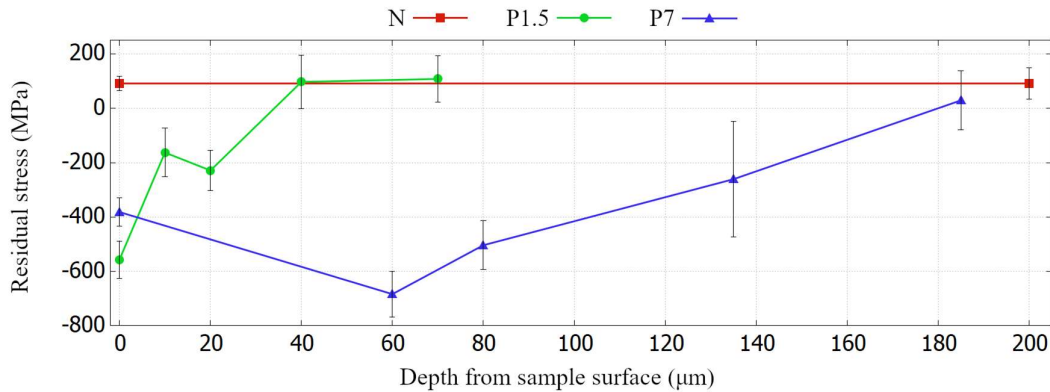


Figure 2. The depth distributions of the residual stresses of $\gamma\text{-Fe}$ in RD.

Fig. 3 shows ODF in $\phi_2 = 45^\circ$ sections for each sample at selected depths. For N sample, the typical rolling texture of face-centred cubic materials was found. Crystallites were oriented along the α -fibre with a dominant Goss ($\{011\}\langle 100\rangle$) and Brass ($\{011\}\langle 211\rangle$) texture components. The Cu ($\{211\}\langle 111\rangle$) texture component was also present with lower intensity. At greater depths, the Brass and Goss components ceased to be resolved and the crystallites were oriented at lower intensities at positions between them. The intensity then increased with increasing depth. For sample P1.5, most of the crystallites had an orientation between Goss and Brass components, which becomes more isolated and intense with increasing depth. In Fig. 3 ODF for sample P1.5 in deeper regions had to be rescaled. The intensities were divided by 10 in order to match the used colour range. The ODF intensity is much higher compared to sample P7. Same as in case of residual stresses, the less intense SP caused greater change in near-surface regions and oriented most of the crystallites to same direction. The surface of sample P7 can be described by the texture along the α -fibre. As with sample N, the predominant crystal orientation was between the Brass

and Goss components. With increasing depth, these texture components began to isolate. For all samples, crystallites were mostly oriented along the incomplete α -fibre. SP caused only a small change in their preferred orientation. That may be explained by the deformation hardening of γ -Fe after rolling, which will thus better resist further deformation caused by SP.

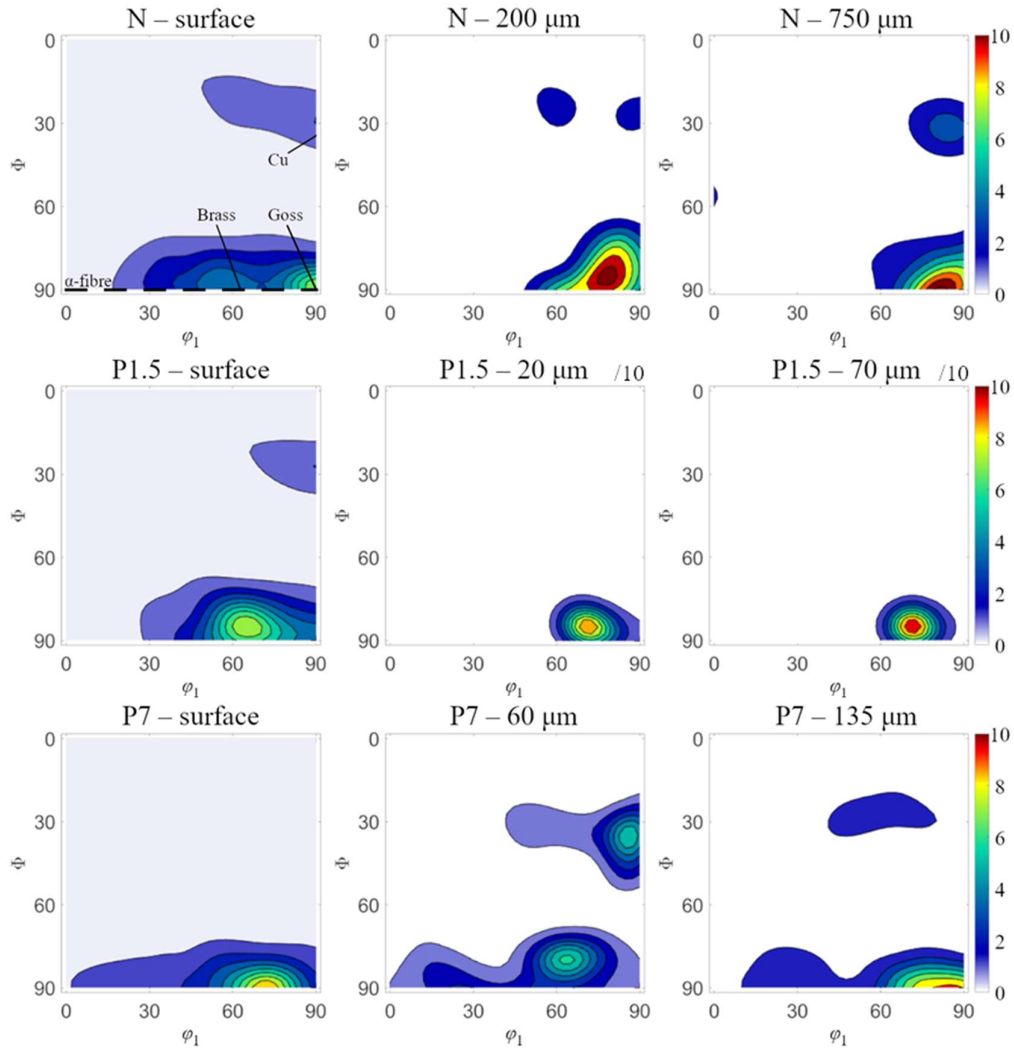


Figure 3. The ODF in $\varphi_2 = 45^\circ$. For sample N, α -fibre represented by dashed line and Goss, Brass, and Cu texture components are shown.

Conclusions

Shot peening alters the real structure parameters of materials which results in a change of their final properties. The effect of shot peening on γ -Fe phase of rolled duplex steel 1.4470 was studied. The main goal was to evaluate the depth distribution of crystallite size, residual stresses, and texture after shot peening with different intensity. Shot peening caused a reduction in crystallite size mostly in near-surface region. With higher intensity, the affected zone increased. Similar effect had shot peening on compressive residual stresses. With higher intensity, the larger stresses deeper in the sample were found. Shot peening with lower intensity caused the biggest change right at the surface of the sample, where compressive residual stresses exceeded values measured for sample P7. Less affected by shot peening was the texture of the samples. Most crystallites only slightly changed their orientation, while remaining in an incomplete α -fibre.

References

- [1] TMR Stainless. Practical Guidelines for the Fabrication of Duplex Stainless Steel. IMO, London, 2014.
- [2] J. Champaine. Shot Peening Overview. *The Shot Peener*, 2001.
- [3] F. Bachman, R. Hielscher, H. Schaeben. Texture Analysis with MTEX – Free and Open Source Software Toolbox. *Solid State Phenomena* **160**: 63-68, 2010

This work was supported by the Grant Agency of the Czech Technical University in Prague, grant No. SGS22/183/OHK4/3T/14.

Automated Image Analysis of exfoliated van der Waals material

Jiří Zelenka^{1,2}, Helena Reichlová², Monika Kučeráková¹, Dominik Kriegner²

¹Department of Solid State Engineering, Faculty of Nuclear Sciences and Physical Engineering,
Czech Technical University in Prague

²Department of Spintronics and Nanoelectronics, Institute of Physics of the Czech Academy of
Sciences
zelenji8@fjfi.cvut.cz

Abstract

Van der Waals materials, like graphene or transition metal dichalcogenides, are very promising for the field of spintronics due to their unique properties. Fabricating devices from these materials requires isolating well defined flakes, a process typically done manually via scotch tape exfoliation and microscopy. This approach is labor-intensive and limited in scope. We introduce a software tool that automates flake identification from microscope images, allowing for rapid and accurate analysis of larger areas. This advancement streamlines the fabrication process and supports the development of high-performance spintronic devices.

Keywords: Software Automatization, Python, Van der Waals Materials, TaRhTe₄, Device Fabrication

Introduction

Van der Waals (vdW) materials, consisting of atomically thin layers held together by weak van der Waals forces, have become central to advancements in spintronics and other emerging technologies due to their exceptional electronic, optical, and mechanical properties. These materials, including graphene, transition metal dichalcogenides, or hexagonal boron nitride, are particularly promising for spintronics, which leverages electron spin in addition to charge to enable faster and more efficient information processing [1].

A key challenge in fabricating devices from these materials is the isolation of a well defined, thin flakes from bulk crystals. The widely used scotch tape exfoliation method, shown in Figure 1, involves applying adhesive tape to a bulk vdW crystal and then peeling it away to transfer thin layers onto a silicon substrate [2]. These layers are subsequently characterized and processed to create functional devices [3]. The process of making electrical contacts to these flakes is crucial, whether for measuring fundamental properties or integrating them into functional devices, such as transistors. This step is complex and requires precision identifying a suitable flake which is sufficiently isolated to provide sufficient space for the lithographic processing.

Currently, the selection of suitable flakes for device fabrication is a labor-, and time-intensive task. Researchers manually examine microscope images to determine flake size, thickness, and morphology, which limits the scope and efficiency of the process. To address this, we present a software tool that automates the identification of vdW flakes from microscope images. This tool significantly speeds up the analysis and allows for the examination of much larger substrate areas. Our software enhances the flake selection process, which is particularly beneficial for working with materials known for their unique electronic properties.

In this work, we test our approach on a vdW compound that hosts type II Weyl nodes—topological features that offer promising electronic properties [4, 5]. By improving the efficiency of flake selection, our tool supports the advancement of devices utilizing these unique materials, facilitating both fundamental characterization and the development of functional spintronic devices.

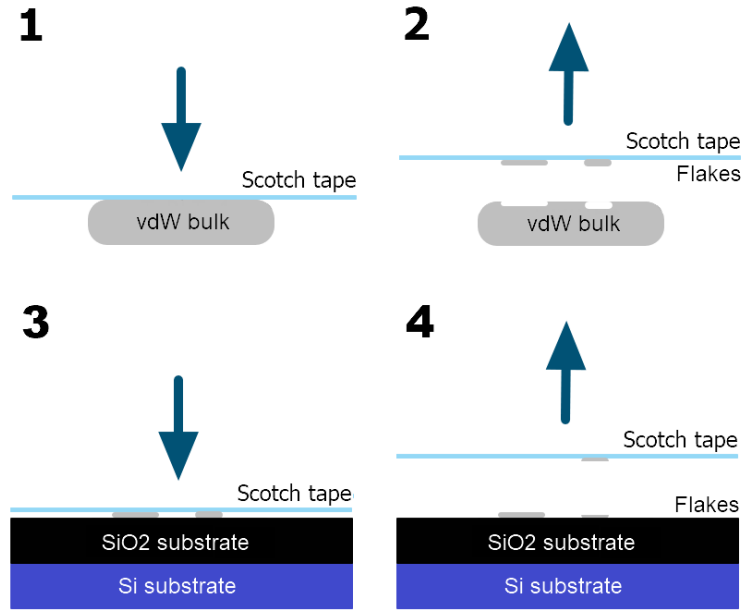


Figure 1: Scotch tape exfoliation of thin van der Waals (vdW) flakes onto a thermally oxidized silicon (Si) substrate. The process is illustrated in four steps: 1) Applying scotch tape to a bulk vdW crystal. 2) Removing the tape with attached flakes. 3) Transferring the flakes onto the substrate. 4) Carefully peeling off the tape to release the flakes.

Test Material for Flake Identification

To test our software, we use exfoliated flakes of TaRhTe_4 , a low-energy topological material known for its four type-II Weyl nodes when in thin-layer form. Raman spectroscopy has confirmed the presence of Weyl fermions in this material, indicated by the absence of inverse symmetry. These fermions disrupt Lorentz covariance in type-II Weyl semimetals [6].

The TaRhTe_4 bulk is grown from tellurium (Te) flux and provided by collaborators at the Leibniz Institute for Solid State and Materials Research - IFW Dresden, Germany. The synthesis involves heating a mixture of tantalum (Ta), rhodium (Rh), and tellurium powders to $1000\text{ }^\circ\text{C}$ and then cooling it to $700\text{ }^\circ\text{C}$ [7]. The crystal structure, detailed in Figure 2, belongs to the orthorhombic $\text{Pmn}2_1$ space group. Rietveld analysis yields the following lattice parameters: $a = 3.75670(11)\text{ \AA}$, $b = 12.5476(5)\text{ \AA}$, and $c = 13.166(3)\text{ \AA}$. For flake separation, the (001) and (010) planes are ideal due to their cleavage properties [8].

To identify suitable flakes for further investigation, we employ the scotch tape exfoliation technique. This method involves applying adhesive tape to the bulk TaRhTe_4 crystal and carefully peeling it away to transfer thin layers onto a substrate. This process allows us to isolate and analyze flakes with the desired properties for subsequent experiments [2].

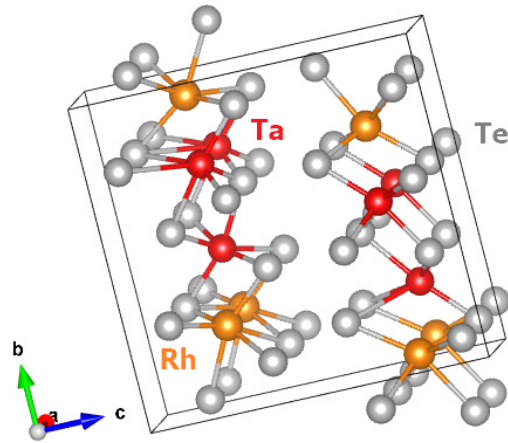


Figure 3: TaRhTe₄ lattice. Parameters were adopted from [8]

Criteria for Flake Detection

For effective device fabrication, the ideal van der Waals flakes should possess the following properties: good crystallinity, thin and uniform thickness, isolated position with respect to other objects.

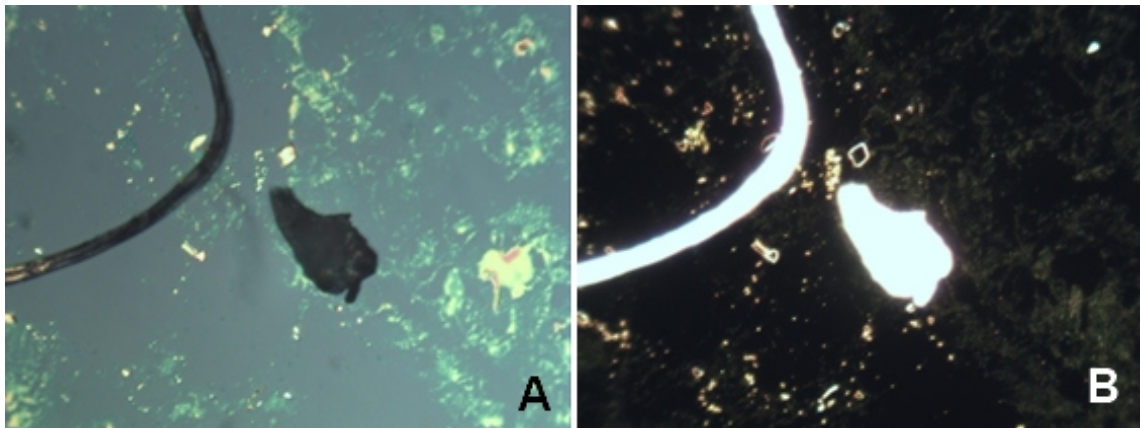


Figure 3: Example photo of substrate with flakes in bright-field (left) and dark-field mode (right) with 20× zoom taken by the microscope camera. There are flakes, adhesive, and impurities.

Figure 3A shows a microscope image of a substrate with flakes, adhesive residue, and other impurities. Similar images are commonly used to identify suitable flakes by manual inspection. In our tests, however, we identified that to improve contrast and differentiate between glue residuals, irregular objects, and the best vdW flakes dark-field microscope images are more suitable. This imaging technique enhances the visibility of flake contours, both thin and thick, while making impurities and adhesive residues more distinguishable against the background. In these dark field images (Figure 3B) the desired vdW flakes with homogeneous thickness are indicated only by their outlines. Straight outlines and 90-degree corners (due to the orthorhombic symmetry of the material) indicate a good crystallinity of the objects.

Figure 4 presents four frames of isolated flakes. Three frames do not contain suitable flakes as they fail to meet the established criteria (Figures 4A, 4C, and 4D). Frame 4B includes one defective flake (top) and one suitable flake (bottom).

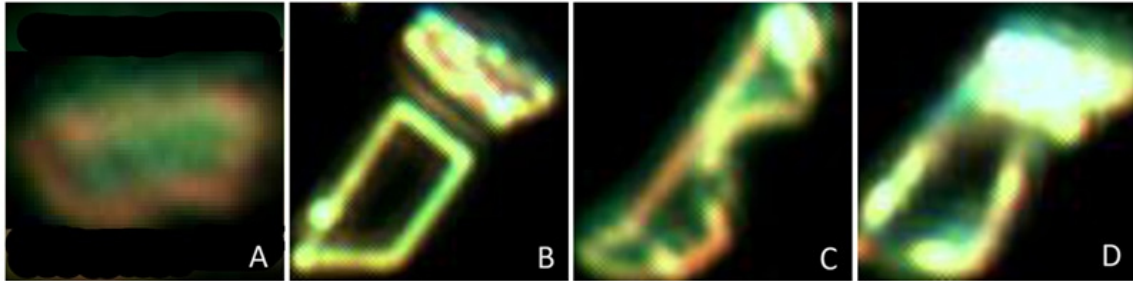


Figure 4: Illustration of a suitable flake (B) and various defects in flakes (A, C, and D). Frame A shows a flake lacking uniform thickness. Frame C depicts a flake without orthorhombic symmetry. Frame D displays two connected flakes. Images were captured using a microscope camera in dark-field mode.

Automatization of the flake detection

We developed software for detecting candidates to suitable flakes for following analysis in object-orientated Python 3. The software is available at GitHub and provides a graphical user interface (Figure 5) and terminal version (Figure 6) While both versions can be used interactively the terminal version can be also used in batch processes using various command line arguments. Installation files and a user manual are provided at <https://github.com/dkrieger/micro-flakes/>.

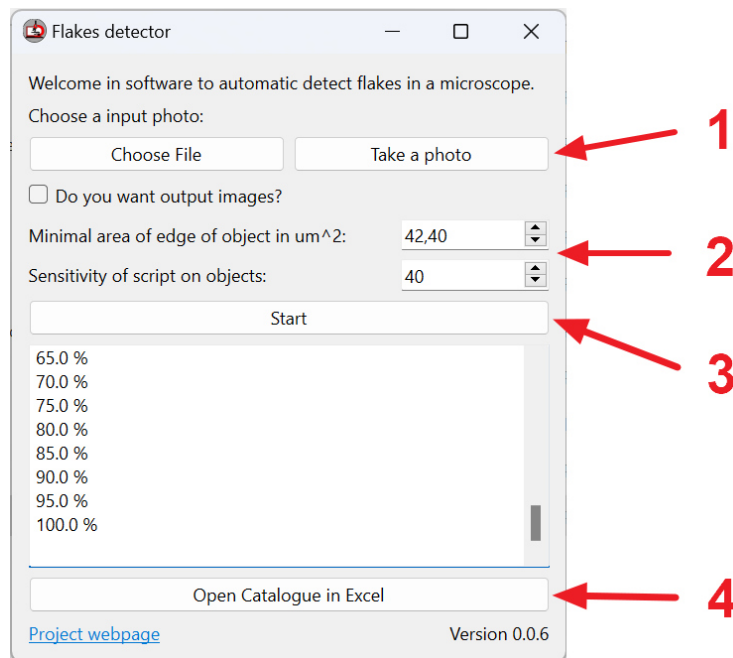


Figure 6: Screenshots of the graphical version of the flake classification software. The process involves four steps: 1) selecting the source of the input photo, 2) setting sensitivity and minimum flake size, 3) initiating the search process, and 4) opening the output catalog in an MS Excel table.

```

C:\Users\jirka\output\termina x + v
Welcome in software to automatics detect object in microscope.
Project webpage: https://github.com/dkriegner/micro-flakes/tree/main/Detector
Version: 0.0.7

Working path: C:\Users\jirka\Documents\Test\input
Do you change the path? [y/N]:
You can upload existing photo or take a new photo by webcam.
Do you upload existing photo? [Y/n]:
Files in input:
['black3.jpg', 'calibration.jpg', 'input', 'output', 'Samle1.jpg', 'Test.jpg', 'Test6.jpg']
Write name of photo from microscope.
../calibration.jpg
Do you want to get image output after 1st iteration? [y/N]:
Write minimal area of edge of object in um^2. Smaller object will be deleted [42.4]:
Write sensitivity of script on objects in dark field. Script will mark all pixels with RGB values bigger than
the user's input. [40]:

```

Figure 5: Screenshots of the terminal version of the flake classification software. Users must select a working directory, choose an image file or capture a new photo, and set the minimum flake size and sensitivity.

The software algorithm operates in two steps. In the first step, it colorizes light pixels (Figures 8a–8b) and divides the image into 7×7 pixels groups. If a group contains more than 70% colored pixels, the entire group is colorized; otherwise, the group is removed (Figure 8c). Small objects (10×10 μm) are deleted, and the centers of gravity are determined (Figure 8d). In the second step, the first step is repeated at a higher resolution (3×3 pixels). Finally, a catalog is created in MS Excel (Figure 9).

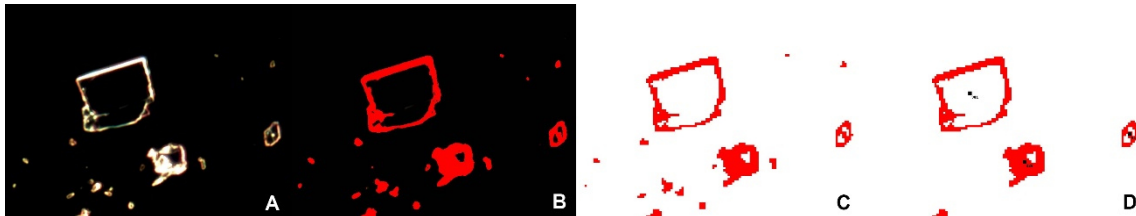


Figure 8: Algorithms in our software for selecting suitable flakes. There is the original photo on the left and the photo with a candidate selecting suitable flakes with ideal size on the right.

The output catalog includes the identification number, x and y coordinates (originating from the top left corner), area in μm², transparency (ratio of dark to total pixels in the flake), estimated size ratio (calculated by equations for rectangle from circumference and area), flake photo, brightness (mean RGB value), contour (ratio of light pixels to circumference), and estimated height (calculated from the linear relationship between brightness and measured height by Dektak Stylus Profilometer).

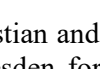
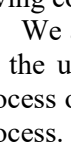
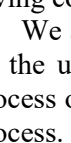
	A	B	C	D	E	F	G	H	I	J	K	L	M	N	O
1	id	x (um)	y (um)	size (um ²)	transparei	size ratio	photo	contourI	contourII	filter - con	Value - big	filter - trar	Value - big	Bright	Height
2	1	31,603	104,907	1,261875	-0,0491	210,9617		202	994	OK	0,670792	NO		492,2709	2905,419
3	2	45,815	353,617	1,25832	-0,04762	193,8996		256	1130	OK	0,164063	NO		435,8182	1776,364
4	3	115,379	265,727	1,340765	0,381387	417,4173		869	4833	NO		OK	0,301387	463,3355	2326,711

Figure 9: Screenshot of the initial section of the flake catalog. It includes ID, x and y coordinates, size, transparency percentage, height/width ratio, contour contrast and intensity, and estimated height.

Discussion

The flake identification software proves highly effective, especially considering that many researchers typically locate flakes on the substrate manually. Using a 20× magnification, each frame covers an area of 500(10)×375(10) μm, within which approximately 400–500 flakes are visible. Our software identified 30, 19, and 20 candidate flakes in three trials, of which 5, 4, and 5 flakes (16–21% of found flakes), respectively, were suitable for lithography. The software significantly reduces the number of flakes to be inspected manually to less than one-tenth, thus saving considerable time.

We are also working on automating the microscope stage, as it is currently moved manually by the user. Capturing the entire substrate requires approximately 100 frames. We are in the process of securing a motorized stage, which the software will control to streamline the imaging process.

In future developments, we plan to integrate a neural network to automate the final decision on flake suitability, further minimizing user involvement. And eventually automate also the design of electrical contacts to the selected flake.

Conclusions

We developed software capable of reducing the number of candidate flakes to less than one-tenth of the total. The software generates an MS Excel table cataloging the potential flakes along with their physical properties and the location on the substrate.

The selected flakes are used to fabricate electronic devices via electron-beam lithography, enabling measurements of their electrical properties. Additionally, we plan to conduct electron diffraction on the flakes using transmission electron microscopy (TEM) for structural analysis.

Acknowledgement

We would like to thank Iryna Galstian and Mahdi Behnami from the Leibniz Institute for Solid State and Materials Research Dresden for their assistance in preparing thin-layer samples of TaRhTe₄. This research was supported by the Grant Agency of the Czech Technical University in Prague under grant No. SGS22/183/OHK4/3T/14.

References

- [1] BISWAL, Bubunu; MISHRA, Shashi B.; YADAV, Renu; POUDYAL, Saroj; RAJARAPU, Ramesh et al. Work function of van der Waals topological semimetals: Experiment and

- theory. Online. Applied Physics Letters. 2022, roč. 120, č. 9. [cit. 2024-08-03]. ISSN 0003-6951. DOI:10.1063/5.0079032.
- [2] LIU, Xinling, Xiaomin YANG, Weihui SANG, Hai HUANG, Wenwu LI, Yen-Fu LIN a Junhao CHU. Thin-film electronics based on all-2D van der Waals heterostructures. Journal of Information Display [on-line]. 2021, 2021-10-02, 22(4), 231-245 [cit. 2024-07-30]. ISSN 1598-0316. DOI:10.1080/15980316.2021.1982782
- [3] AJAYAN, Pulickel, Philip KIM, Kaustav BANERJEE, et al. Two-dimensional van der Waals materials. Physics Today [online]. 2016, 2016-09-01, 69(9), 38-44 [cit. 2024-04-01]. ISSN 0031-9228. DOI:10.1063/PT.3.3297
- [4] JIANG, Qianni, Johanna C. PALMSTROM, John SINGLETON, et al. Nature Communications [online]. 2024, 15(1) [cit. 2024-04-12]. ISSN 2041-1723. DOI:10.1038/s41467-024-46633-w
- [5] KOEPERNIK, K., D. KASINATHAN, D. V. EFREMOV, Seunghyun KHIM, Sergey BORISENKO, Bernd BÜCHNER a Jeroen VAN DEN BRINK. TaIrTe₄: A ternary type-II Weyl semimetal. Physical Review B [online]. 2016, 93(20) [cit. 2024-03-28]. ISSN 2469-9950. DOI:10.1103/PhysRevB.93.201101
- [6] LAI, Jiawei, Yinan LIU, Junchao MA, et al. Broadband Anisotropic Photoresponse of the “Hydrogen Atom” Version Type-II Weyl Semimetal Candidate TaIrTe₄. ACS Nano [online]. 2018, 2018-04-24, 12(4), 4055-4061 [cit. 2024-04-01]. ISSN 1936-0851. Dostupné z: doi:10.1021/acsnano.8b01897
- [7] HAUBOLD, E., K. KOEPERNIK, D. EFREMOV, et al. Physical Review B [online]. 2017, 95(24) [cit. 2024-04-01]. ISSN 2469-9950. DOI:10.1103/PhysRevB.95.241108
- [8] SHIPUNOV, G., B. R. PIENING, C. WUTTKE, et al. Layered van der Waals Topological Metals of TaTMTe₄ (TM = Ir, Rh, Ru) Family. The Journal of Physical Chemistry Letters [online]. 2021, 2021-07-22, 12(28), 6730-6735 [cit. 2024-04-07]. ISSN 1948-7185. DOI:10.1021/acs.jpcclett.1c01648

Program konference S2PAM13

	Úterý 3.9.2024	Středa 4.9.2024	Čtvrtek 5.9.2024	Pátek 6.9.2024	
7:30 – 9:00		snídaně	snídaně	snídaně	
9:00 – 9:25		Zajac	Mascaretti	Špetík	
9:25 – 9:35		Meřová	Kolář	Čtvrtlík	
9:35 – 9:50		Samochvalova	Correa		Dráb
9:50 – 10:10				Coffee break	
10:10 – 10:15		Skočdopole	Kučeráková	Trojan	
10:15 – 10:25		Jůza	Kwiecien	Rušin	
10:25 – 10:35		Lojka	Červenka	Čapek	
10:35 – 10:45		Sulovský		Oběd	Conference closing
10:45 – 10:55		Oběd	Lis	Oběd	
10:55 – 11:00				Batysta	Kukal
11:00 – 11:10		Conference opening			
11:10 – 11:20		Kušnír		Gašpar	
11:20 – 11:25		Kahan			Coffee break
11:25 – 11:45		Burda		Hamrle	
11:45 – 11:50		Kalvoda		Matoušková	
11:50 – 12:10		Zelenka			
12_10 - 12:15		večeře		večeře	večeře
12:15 – 14:00					
14:00-14:25					
14:25 - 14:50					
14:50 – 15:00					
15:00 – 15:10					
15:10 – 15:25					
15:25 – 15:35					
15:35 – 15:50					
15:50 – 15:55					
15:55 – 16:10					
16:10 – 16:20					
16:20 – 16:35					
16:35 – 16:55					
16:55 – 17:10					
18:30					

Sekce:	Chairman:		Sekce:	Chairman:
	<i>Kalvoda</i>			<i>Correa</i>
	<i>Kučeráková</i>			<i>Skočdopole</i>
	<i>Kalvoda</i>			<i>Hamrle</i>
	<i>Čapek</i>			<i>Kalvoda</i>
	<i>Kwiecien</i>			<i>Kušnír</i>

Autor (editor): K. Aubrechtová Dragounová, M. Kučeráková, L. Kalvoda, J. Čapek, K. Trojan
Název díla: Sborník příspěvků 13. studentské vědecké konference fyziky pevných látek,
fotoniky a materiálů, Nové Hrady 2024
V roce 2024 vydalo České vysoké učení technické v Praze
Zpracovala Fakulta jaderná a fyzikálně inženýrská
Kontaktní adresa: Trojanova 13, 120 00 Praha 2
Tel.: +420 22435 8611
Vydání: 1.
Tisk: powerprint s. r. o.
Adresa tiskárny: Brandejsovo nám. 1219/1, 16500 Praha 6 Suchdol
Počet stran: 67
ISBN 978-80-01-07382-7